



UNIVERSITY OF LEEDS

This is a repository copy of *Extreme enriched and heterogeneous $^{87}\text{Sr}/^{86}\text{Sr}$ ratios recorded in magmatic plagioclase from the Samoan hotspot.*

White Rose Research Online URL for this paper:
<http://eprints.whiterose.ac.uk/144146/>

Version: Accepted Version

Article:

Edwards, MA, Jackson, MG, Kylander-Clark, ARC et al. (8 more authors) (2019) Extreme enriched and heterogeneous $^{87}\text{Sr}/^{86}\text{Sr}$ ratios recorded in magmatic plagioclase from the Samoan hotspot. *Earth and Planetary Science Letters*, 511. pp. 190-201. ISSN 0012-821X

<https://doi.org/10.1016/j.epsl.2019.01.040>

© 2019 Elsevier B.V. This manuscript version is made available under the CC-BY-NC-ND 4.0 license <http://creativecommons.org/licenses/by-nc-nd/4.0/>.

Reuse

This article is distributed under the terms of the Creative Commons Attribution-NonCommercial-NoDerivs (CC BY-NC-ND) licence. This licence only allows you to download this work and share it with others as long as you credit the authors, but you can't change the article in any way or use it commercially. More information and the full terms of the licence here: <https://creativecommons.org/licenses/>

Takedown

If you consider content in White Rose Research Online to be in breach of UK law, please notify us by emailing eprints@whiterose.ac.uk including the URL of the record and the reason for the withdrawal request.



eprints@whiterose.ac.uk
<https://eprints.whiterose.ac.uk/>

Extreme enriched and heterogeneous $^{87}\text{Sr}/^{86}\text{Sr}$ ratios recorded in magmatic plagioclase from the Samoan hotspot

M.A. Edwards^{1*}, M.G. Jackson¹, A.R.C. Kylander-Clark¹, J. Harvey², G.A. Hagen-Peter³, G.G.E. Seward¹, C.B. Till⁴, J.V. Adams¹, J.M. Cottle¹, B.R. Hacker¹, F.J. Spera¹

¹Department of Earth Science, University of California Santa Barbara, Santa Barbara, CA 93106, USA (*Corresponding author)

²School of Earth and Environment, University of Leeds, Leeds LS2 9JT, UK

³Center for Earth System Petrology, Department of Geoscience, Aarhus University, 8000 Aarhus C, Denmark

⁴School of Earth & Space Exploration, Arizona State University, Tempe, AZ 85287, USA

Abstract

We report the major-element, trace-element, and $^{87}\text{Sr}/^{86}\text{Sr}$ compositions of six plagioclase crystals from two Samoan lavas with extreme EM2 isotopic compositions (ALIA-115-18 with whole-rock $^{87}\text{Sr}/^{86}\text{Sr}$ of 0.718592, and ALIA-115-21 with whole-rock $^{87}\text{Sr}/^{86}\text{Sr}$ of 0.720469). We employed laser-ablation split-stream mass spectrometry (LASS) to simultaneously measure $^{87}\text{Sr}/^{86}\text{Sr}$ ratios, major-element, and trace-element concentrations in the same plagioclase crystal volume. We find that two plagioclase crystals have extreme $^{87}\text{Sr}/^{86}\text{Sr}$ heterogeneity in excess of 5000 ppm (where ppm of $^{87}\text{Sr}/^{86}\text{Sr}$ variability = $10^6 \cdot [^{87}\text{Sr}/^{86}\text{Sr}_{\text{max}} - ^{87}\text{Sr}/^{86}\text{Sr}_{\text{min}}] / ^{87}\text{Sr}/^{86}\text{Sr}_{\text{avg}}$). In two of the plagioclase crystals, we identify the highest $^{87}\text{Sr}/^{86}\text{Sr}$ ratios (0.7224) ever measured in any fresh, mantle-derived ocean island basalt (OIB) or OIB-hosted mineral phase.

We find that in $^{87}\text{Sr}/^{86}\text{Sr}$ -versus-Sr concentration space, the six plagioclase crystals overlap in a “common component” region with higher $^{87}\text{Sr}/^{86}\text{Sr}$ than has been previously identified in whole-rock Samoan lavas or mineral separates. We use the occurrence of olivine mineral inclusions ($\text{Fo} = 74.5 \pm 0.8$, 2 SD) in the high- $^{87}\text{Sr}/^{86}\text{Sr}$ zone of one plagioclase crystal to infer the bulk composition ($\text{Mg}\# = 46.8 \pm 0.8$, 2 SD) of the extreme EM2 magma from which the olivine and high- $^{87}\text{Sr}/^{86}\text{Sr}$ plagioclase crystallized. We argue that a relatively evolved EM2

endmember magma mixed with at least one lower- $^{87}\text{Sr}/^{86}\text{Sr}$ melt to generate the observed intra-crystal plagioclase isotopic heterogeneity.

By inferring that subducted terrigenous sediment gives rise to EM2 signatures in Samoan lavas, we estimate that the quantity of sediment necessary to generate the most-elevated $^{87}\text{Sr}/^{86}\text{Sr}$ ratios observed in the Samoan plagioclase is ~7% of the mantle source. We also estimate that sediment subduction into the mantle over geologic time has generated a sediment domain that constitutes 0.02% of the mass of the mantle, a much lower proportion than required in the EM2 mantle source. Even if subducted sediment is concentrated in large low-shear-velocity provinces (LLSVPs) at the base of the mantle (which constitute up to 7.7% of the mantle's mass), then only 0.25% of the LLSVPs are composed of sediment. This requires that the distribution of subducted sediment in the mantle is heterogeneous, and the high relative abundance of sediment in the Samoan EM2 mantle is an anomalous relic of ancient subduction that has survived convective attenuation.

Highlights

- Highest $^{87}\text{Sr}/^{86}\text{Sr}$ reported in fresh OIB or OIB-hosted phase (0.72239) to date.
- Significant (> 5000 ppm) $^{87}\text{Sr}/^{86}\text{Sr}$ intra-grain heterogeneity measured in plagioclase.
- Geochemical data suggest a common EM2 endmember is sampled by Samoan plagioclase.
- Extreme EM2 melt in equilibrium with olivine inclusions in plagioclase is relatively evolved.
- The mantle source of extreme EM2 melt requires approximately 7% recycled terrigenous sediment.

1. Introduction

The observation that ocean island basalts (OIB) show variations in radiogenic isotopic compositions suggests that the mantle is heterogeneous (e.g., Gast et al., 1964; Hart et al., 1973; Zindler and Hart, 1986; Hofmann, 1997; Stracke, 2012; White, 2015). Globally, OIB can be grouped into distinct end-members defined by their Sr, Nd, and Pb isotopic compositions: i) depleted MORB mantle, ii) “high μ ” = $^{238}\text{U}/^{204}\text{Pb}$, iii) enriched mantle 1, and iv) enriched mantle 2 (DMM, HIMU, EM1 and EM2, respectively; Zindler and Hart, 1986). Although it is clear that isotopic differences exist in OIB, the origins, geometries, and ages of the isotopic “domains” in Earth’s mantle remain active areas of inquiry.

Studies of mantle-derived lavas most often employ whole-rock isotopic measurements, which homogenize any isotopic heterogeneity that may exist among different phases or within individual minerals (or melt inclusions) in a lava. Although whole-rock analyses can be useful in identifying large-scale isotopic heterogeneities in Earth’s mantle (e.g., Hofmann, 1997; Stracke, 2012; White, 2015), information about possible isotopic heterogeneity within a single lava is lost (e.g., Davidson et al., 2007).

Previous work has identified $^{87}\text{Sr}/^{86}\text{Sr}$ disequilibrium between olivine-hosted melt inclusions and their host oceanic lavas, an observation that suggests that multiple isotopically distinct melt sources may contribute to a single lava (or that the assimilation of crust modifies the isotopic composition of lavas after olivine crystallization) (e.g., Harlou et al., 2009; Jackson and Hart, 2006; Reinhard et al., 2016, 2018; Sobolev et al., 2011). Lead isotopic variability has also been observed in olivine-hosted melt inclusions in OIB (Saal et al., 1998; Yurimoto et al., 2004; Sobolev et al., 2011), although the extent of this variability has been debated (Paul et al., 2011).

Furthermore, the Sr, Nd, Hf, and Pb isotopic compositions of clinopyroxene hosted in OIB lavas have been demonstrated to be in isotopic disequilibrium with their host whole rocks (Hanyu and Nakamura, 2000; Jackson et al., 2009; Hanyu et al., 2011; Miyazaki et al., 2018). These studies collectively suggest that intra-lava isotopic heterogeneity exists in some OIB. However, the mechanisms for generating this heterogeneity remain unresolved.

Plagioclase is well suited to evaluating the nature and origin of $^{87}\text{Sr}/^{86}\text{Sr}$ heterogeneity in OIB lavas because i) Sr is compatible in plagioclase, so plagioclase has elevated Sr concentrations relative to the bulk rock; ii) plagioclase has low Rb concentrations, thereby minimizing the impact of the isobaric interference of ^{87}Rb on mass 87 when employing in situ analytical methods; iii) plagioclase can contain domains (or zones) with distinct $^{87}\text{Sr}/^{86}\text{Sr}$ compositions (Christensen et al., 1995; Davidson and Tepley, 1997; Ramos et al., 2005; Font et al., 2008; Lange et al., 2013); and iv) $^{87}\text{Sr}/^{86}\text{Sr}$ compositions can be linked to the major- and trace-element compositional domains in the plagioclase. Such domains record a “crystal stratigraphy” that can provide relative temporal information (from plagioclase core to rim) about the processes that contributed to the isotopic composition of a single plagioclase crystal.

To our knowledge, intra-crystal $^{87}\text{Sr}/^{86}\text{Sr}$ zonation has not been reported in plagioclase in OIB. Therefore, this study uses LASS (laser-ablation split-stream mass spectrometry; Kylander-Clark et al., 2013) to measure the $^{87}\text{Sr}/^{86}\text{Sr}$ and major- and trace-element compositions of six plagioclase crystals hosted in two extreme EM2 lavas from the Samoan hotspot with the most elevated $^{87}\text{Sr}/^{86}\text{Sr}$ signatures ever reported in global OIB (with whole-rock $^{87}\text{Sr}/^{86}\text{Sr}$ of 0.718592 and 0.720469; Jackson et al., 2007).

2. Sample description and methods

2.1. Sample description and EPMA analysis

We targeted two lavas from the Samoan hotspot—ALIA-115-18 and ALIA-115-21—that have previously been characterized for whole-rock isotopic, major-element, and trace-element geochemistry. ALIA-115-18 and ALIA-115-21—a trachybasalt and trachyandesite, respectively—were dredged aboard the R/V Kilo Moana in April 2005 from the deep (3220 m below sea level) southwest flank of Savai'i Island, western Samoa (Figure 1) (Jackson et al., 2007; Koppers et al., 2008). A suite of five rocks from ALIA dredge 115 range in age from 4.98 to 5.06 Ma (Koppers et al., 2008). ALIA-115-18 (whole-rock $^{87}\text{Sr}/^{86}\text{Sr}$ is 0.718592) and ALIA-115-21 (whole-rock $^{87}\text{Sr}/^{86}\text{Sr}$ is 0.720469; Jackson et al., 2007) have the most geochemically enriched $^{87}\text{Sr}/^{86}\text{Sr}$ signatures measured in whole-rock OIB to date (Figure 2). Previous work on samples ALIA-115-18 and ALIA-115-21 also revealed significant $^{87}\text{Sr}/^{86}\text{Sr}$ disequilibrium (up to 3115 ppm and 1611 ppm, respectively) between clinopyroxene and the host whole rocks (Jackson et al., 2009), making these two samples ideal targets for investigating $^{87}\text{Sr}/^{86}\text{Sr}$ heterogeneity in OIB-hosted plagioclase. ALIA-115-18 and ALIA-115-21 host large, mm-scale plagioclase crystals (see electron probe microanalysis [EPMA] images in Supplementary Figure 1) that were targeted here. See the Supplementary Methods for a description of sample preparation, EPMA mapping of the plagioclase crystals, and EPMA analysis of olivine inclusions in plagioclase ALIA-115-18-1 (Table 1).

2.2. Laser ablation split-stream mass spectrometry

We employed LASS (laser-ablation split-stream mass spectrometry; Kylander-Clark et al., 2013) to simultaneously measure major- and trace-element concentrations and $^{87}\text{Sr}/^{86}\text{Sr}$ compositions of Samoan plagioclase. This analytical approach couples a Teledyne CETAC

Photon Machines Analyte 193 nm ArF excimer laser and HelEx sample cell to two mass spectrometers: a Nu Instruments Plasma HR multi-collector inductively coupled plasma mass spectrometer (MC-ICP-MS) for $^{87}\text{Sr}/^{86}\text{Sr}$ measurements, and an Agilent 7700X quadrupole inductively coupled plasma mass spectrometer (Q-ICP-MS) for trace-element concentration measurements. The ablated sample is mixed in a mixing bulb; the sample flow path is then split such that approximately half of the sample is directed to each mass spectrometer. The LASS facility at the University of California at Santa Barbara is described in detail by Kylander-Clark et al. (2013).

LASS enables investigation of the relationships between $^{87}\text{Sr}/^{86}\text{Sr}$ and plagioclase major- and trace-element geochemistry from the same laser spot, and thereby facilitates the interpretation of isotopic data. Additionally, LASS allows filtering or discarding of $^{87}\text{Sr}/^{86}\text{Sr}$ analyses that contain inclusions or other phases. As a result, LASS allows targeting of phase-specific $^{87}\text{Sr}/^{86}\text{Sr}$ data by identifying and discarding isotopic data associated with non-plagioclase trace-element signatures (Figure 3). For each ALIA-115 plagioclase crystal, data from multiple spot analyses on each crystal were used to generate a model $^{87}\text{Sr}/^{86}\text{Sr}$ and Sr concentration surfaces using Matlab[®] (Figure 4 and Supplementary Figure 2).

2.2.1. LASS $^{87}\text{Sr}/^{86}\text{Sr}$ measurements

The $^{87}\text{Sr}/^{86}\text{Sr}$ composition of plagioclase can be measured using LA-MC-ICP-MS with sufficient precision to resolve isotopic variability, though complicating factors include instrumental mass fractionation and isobaric interferences (Davidson et al., 2007). In practice, mass fractionation can be corrected by monitoring deviations from a canonical $^{86}\text{Sr}/^{88}\text{Sr}$ stable isotope ratio (0.1194), and correcting the measured $^{87}\text{Sr}/^{86}\text{Sr}$ ratio using the exponential mass

fractionation law. However, isobaric interferences on mass 86 from ^{86}Kr (present as a contaminant in the Ar carrier gas) can result in inaccurate measured $^{86}\text{Sr}/^{88}\text{Sr}$ and $^{87}\text{Sr}/^{86}\text{Sr}$ ratios. Therefore, in this study the Kr correction approach described by Konter and Storm (2014) was implemented to correct for Kr interferences. For a detailed description of this correction algorithm and of the MC-ICP-MS analytical procedures employed in this study, refer to Konter and Storm (2014) and the Supplementary Methods.

After correction for isobaric interferences (Kr and Rb; see Supplementary Methods) and mass fractionation, we used an in-house plagioclase primary reference material to correct the measured $^{87}\text{Sr}/^{86}\text{Sr}$ ratios of samples and secondary reference materials. This primary reference material, T21 (a homogenized plagioclase glass), was prepared by separating 450 mg of inclusion-free plagioclase chips from plagioclase-rich Samoan basalt sample T21 (see Workman et al., 2004). The plagioclase chips were powdered to $< 40 \mu\text{m}$ and fused twice in a $1500 \text{ }^\circ\text{C}$ furnace at Arizona State University, resulting in a homogeneous plagioclase glass (see Supplementary Table 1 for the major-element composition and Supplementary Table 2 for the trace-element composition of T21). The $^{87}\text{Sr}/^{86}\text{Sr}$ value of T21—determined via TIMS at the University of Leeds and corrected to an NBS987 $^{87}\text{Sr}/^{86}\text{Sr}$ value of 0.710240—is 0.704712 ± 0.000009 (2 SE) (see Table 2), similar to the whole-rock $^{87}\text{Sr}/^{86}\text{Sr}$ value of T21 (0.704751; Workman et al., 2004). The offset between the preferred TIMS and measured LASS $^{87}\text{Sr}/^{86}\text{Sr}$ values for T21 is calculated, and this offset (or “correction factor”) is applied to all secondary reference materials and plagioclase samples using a linear interpolation. Following application of the correction factor, the secondary reference materials measured during the course of this study yield accurate $^{87}\text{Sr}/^{86}\text{Sr}$ ratios (see below).

Secondary reference materials for $^{87}\text{Sr}/^{86}\text{Sr}$ used in this study include a naturally homogeneous plagioclase crystal from the American Museum of Natural History, AMNH 107160 plagioclase ($^{87}\text{Sr}/^{86}\text{Sr} = 0.704386 \pm 0.000008$ [2 SE] via TIMS, Table 2; see Supplementary Table 1 for major-element analyses and Supplementary Table 2 for trace-element analyses), the USGS MACS-3 carbonate reference material ($^{87}\text{Sr}/^{86}\text{Sr} = 0.707546 \pm 0.000004$ [2 SE] via TIMS; Jochum et al., 2011), and a modern sclerosponge ($^{87}\text{Sr}/^{86}\text{Sr}$ of modern seawater = 0.709164 ± 0.000002 [2 SE] via TIMS; Mokadem et al., 2015). All $^{87}\text{Sr}/^{86}\text{Sr}$ values of the primary and secondary reference materials have been normalized to an NBS987 $^{87}\text{Sr}/^{86}\text{Sr}$ value of 0.710240.

LASS analyses were conducted during three analytical sessions on 3/2/2017, 5/8/2017, and 8/15/2017. A summary of all LASS and TIMS $^{87}\text{Sr}/^{86}\text{Sr}$ analyses of secondary materials—as well as analyses of an OIB-hosted plagioclase with homogeneous $^{87}\text{Sr}/^{86}\text{Sr}$ from Pitcairn sample Pit-16 (Garapić et al., 2015; see Supplementary Methods)—is available in Table 3, and $^{87}\text{Sr}/^{86}\text{Sr}$ (and major- and trace-element) data from each laser spot are available in Supplementary Table 3. Following correction to the preferred T21 value, the mean $^{87}\text{Sr}/^{86}\text{Sr}$ values of the three secondary $^{87}\text{Sr}/^{86}\text{Sr}$ reference materials obtained by LASS agree with the TIMS reference values to better than 33 ppm. Additionally, the reproducibility of measured $^{87}\text{Sr}/^{86}\text{Sr}$ was ± 260 ppm (2 RSD, $n = 40$) for the modern sclerosponge over three analytical sessions, ± 270 ppm (2 RSD, $n = 40$) for MACS-3 over three analytical sessions, and ± 353 ppm (2 RSD, $n = 73$) for AMNH 107160 plagioclase over two analytical sessions. The mean $^{87}\text{Sr}/^{86}\text{Sr}$ value measured by LASS for Pit-16 plagioclase agrees with the value measured for the micromilled powder measured via TIMS within 115 ppm (see Table 3, Supplementary Figure 3, and Supplementary Methods). Reference materials and samples were analyzed identically aside from the laser spot size and repetition rate,

which we varied according to the Sr concentration of the analyte. The T21 primary reference material (1306 ppm Sr; Supplementary Table 2) and the AMNH 107160 secondary reference material (968 ppm) have lower Sr concentrations than the ALIA-115-18 (2054 ± 461 ppm, 2 SD; Supplementary Table 4) and the ALIA-115-21 (2218 ± 656 ppm, 2 SD) plagioclase crystals. During the analytical sessions, we analyzed the T21 and AMNH 107160 plagioclase reference materials every fourth sample analysis, and the MACS-3 and sclerosponge reference materials every twentieth sample analysis.

2.2.2. LASS major- and trace-element measurements

We measured the major- and trace-element compositions of plagioclase by LASS. A detailed description of LASS trace-element measurement procedures and the accuracy and reproducibility of LASS major- and trace-element measurements of reference materials is in the Supplementary Methods. Major- and trace-element concentrations obtained by LASS used ^{43}Ca as an internal standard. For T21 plagioclase, AMNH 107160 plagioclase, Pit-16 plagioclase, and all Samoan plagioclase crystals analyzed by LASS in this study, ^{43}Ca is from EPMA Ca concentration measurements (Supplementary Tables 2–4).

3. Data and observations

We targeted six individual plagioclase crystals from Samoan lava samples ALIA-115-18 and ALIA-115-21. A summary of all $^{87}\text{Sr}/^{86}\text{Sr}$, trace-element, and major-element geochemical data obtained on these plagioclase crystals is in Supplementary Table 4. All $^{87}\text{Sr}/^{86}\text{Sr}$ measurements are summarized in Figure 5, and plagioclase $^{87}\text{Sr}/^{86}\text{Sr}$ results are compared to whole-rock and clinopyroxene $^{87}\text{Sr}/^{86}\text{Sr}$ values previously obtained from samples ALIA-115-18

and ALIA-115-21 (Jackson et al., 2007, 2009). We identify plagioclase domains with $^{87}\text{Sr}/^{86}\text{Sr}$ compositions that extend to values both lower and higher than those identified in host whole rocks and in clinopyroxene from the same lavas (Figure 5). We find significant intra-crystal isotopic heterogeneity in most of the plagioclase crystals that in some cases greatly exceeds the analytical reproducibility of LASS $^{87}\text{Sr}/^{86}\text{Sr}$ measurements of reference materials.

3.1. Description of individual crystals and geochemical characteristics

3.1.1. ALIA-115-18 plagioclase

The three plagioclase crystals from Samoan lava ALIA-115-18 targeted here are approximately 2 mm x 0.5 mm in size and are characterized by the presence of fine oscillatory zoning that is visible in the quantitative EPMA maps of each grain (Supplementary Figure 1). The morphology and geochemical data collected for individual plagioclase crystals from ALIA-115-18 are described below.

ALIA-115-18-1: This plagioclase has a rounded, resorbed core with olivine and clinopyroxene inclusions along the outer edge of the core (see Supplementary Figure 1 for EPMA maps of this crystal). The average anorthite content ($An = \text{molar Ca}/[\text{Ca} + \text{Na}] \cdot 100$) of this crystal at locations corresponding to each of the laser spots is 59 ± 2 (2 SD, using EPMA data compiled in Supplementary Table 4). We measured the $^{87}\text{Sr}/^{86}\text{Sr}$ and trace-element composition of this plagioclase in 75 spot locations over three analytical sessions. This plagioclase exhibits coherent $^{87}\text{Sr}/^{86}\text{Sr}$ zoning: a low- $^{87}\text{Sr}/^{86}\text{Sr}$ core is surrounded by a high- $^{87}\text{Sr}/^{86}\text{Sr}$ mantle, and a thin (c. 100 μm) low- $^{87}\text{Sr}/^{86}\text{Sr}$ rim (Figure 4). Small (c. 20–30 μm) olivine inclusions occur in the plagioclase

within the high- $^{87}\text{Sr}/^{86}\text{Sr}$ zone—called the “olivine-bearing zone” hereafter—near the boundary with the low $^{87}\text{Sr}/^{86}\text{Sr}$ core (Figure 4). The $^{87}\text{Sr}/^{86}\text{Sr}$ values measured in this plagioclase span from 0.71853 ± 0.00032 (2 SE) to 0.72239 ± 0.00027 (2SE); the measured $^{87}\text{Sr}/^{86}\text{Sr}$ range is approximately 5300 ppm. As with the other plagioclase crystals in this study, Sr shows an inverse relationship with $^{87}\text{Sr}/^{86}\text{Sr}$ (see section 3.2 and Figure 6). This anticorrelation is also demonstrated in Figure 4, wherein the low- $^{87}\text{Sr}/^{86}\text{Sr}$ core has elevated Sr concentrations, and the high- $^{87}\text{Sr}/^{86}\text{Sr}$ region has lower Sr concentrations.

The mean $^{87}\text{Sr}/^{86}\text{Sr}$ value of four analyses made from the olivine-bearing zone is 0.72194 ± 0.00057 (2 SE), indistinguishable from (i.e., within uncertainty of) the highest value (0.72239 ± 0.00027 [2 SE]; Supplementary Table 4) reported in this study. We targeted four olivine inclusions with EPMA spot analyses (see Table 1) in order to calculate the equilibrium melt Mg# associated with the olivines. The analyzed olivines have a mean forsterite content (= molar $\text{Mg}/[\text{Mg} + \text{Fe}^{2+}] \cdot 100$) of 74.5 ± 0.8 (2 SD, $n = 14$ measurements from 4 different olivine inclusions). Assuming an olivine-melt K_D of 0.3 (where $K_D = [\text{Fe}^{2+}/\text{Mg}]_{\text{olivine}}/[\text{Fe}^{2+}/\text{Mg}]_{\text{melt}}$; Roeder and Emslie, 1970), this olivine was in equilibrium with a melt with $\text{Mg}\# = 46.8 \pm 0.4$ (2 SD) (where $\text{Mg}\#$ is molar $\text{Mg}/[\text{Mg} + \text{Fe}^{2+}] \cdot 100$). An uncertainty of 10% in the K_D value yields a range in calculated equilibrium $\text{Mg}\#$ of 44 to 49, which is depicted by the error bars shown in Figure 7.

ALIA-115-18-2: Plagioclase ALIA-115-18-2 contains multiple isolated regions of concentric anorthite zoning surrounded by a rim (Supplementary Figure 1). The mean An content of this crystal is 59 ± 3 (2 SD) at the location of the laser spots (see data in Supplementary Table 4). We measured the $^{87}\text{Sr}/^{86}\text{Sr}$ composition of this plagioclase in 52 spot locations over two analytical

sessions on 5/7/2017 and 8/15/2017. EPMA elemental maps of this sample were generated after the first (but before the second) laser ablation analytical session; therefore, we used the mean Ca concentration from the locations of the laser spots from the second analytical session as an internal standard to calculate trace-element concentrations from the first laser-ablation analytical session. Because the Ca concentration for this crystal varies by only 11% (2 RSD; the Ca content at the locations of the laser spots is 8.12 ± 0.45 wt %, 2 SD, $n = 40$), this approximation introduces minimal additional uncertainty to the measured trace-element concentrations. The range (5700 ppm) in $^{87}\text{Sr}/^{86}\text{Sr}$ values measured in this plagioclase (0.71792 ± 0.00028 [2 SE] to 0.72205 ± 0.00024 [2 SE]) is greater than that measured in any of the other plagioclase crystals in this study. This crystal has a core characterized by low $^{87}\text{Sr}/^{86}\text{Sr}$, a mantle with moderate $^{87}\text{Sr}/^{86}\text{Sr}$, and a rim with high $^{87}\text{Sr}/^{86}\text{Sr}$ (Supplementary Figure 2).

ALIA-115-18-3: Plagioclase crystal ALIA-115-18-3 has an irregular core surrounded by a region characterized by oscillatory major-element zoning (Supplementary Figure 1). The An content of this crystal is 58 ± 3 (2 SD, $n = 31$) determined at the location of each of the laser spots (Supplementary Table 4), which is similar to the preceding two ALIA-115-18 plagioclase crystals. We measured the $^{87}\text{Sr}/^{86}\text{Sr}$ and trace-element composition of this crystal in 30 locations over two analytical sessions. The measured $^{87}\text{Sr}/^{86}\text{Sr}$ values in this sample span 0.71789 ± 0.00024 (2 SE) to 0.72111 ± 0.00031 (2 SE); the measured range of $^{87}\text{Sr}/^{86}\text{Sr}$ is approximately 4400 ppm. This crystal has the lowest measured $^{87}\text{Sr}/^{86}\text{Sr}$ in this study (0.71789), but no measured $^{87}\text{Sr}/^{86}\text{Sr}$ values as high as those observed in the other two ALIA-115-18 plagioclase crystals (Figure 5). In contrast to the two previously described crystals from ALIA-115-18, this

crystal contains a core characterized by high $^{87}\text{Sr}/^{86}\text{Sr}$ that is surrounded by a mantle with lower $^{87}\text{Sr}/^{86}\text{Sr}$.

3.1.2. ALIA-115-21 plagioclase

We measured the $^{87}\text{Sr}/^{86}\text{Sr}$, major-element, and trace-element composition of three plagioclase crystals from Samoan lava ALIA-115-21, and found that the crystals exhibit more variability in An content (both higher and lower An values) than the ALIA-115-18 crystals (see lower panel of Figure 6). Additionally, although the ALIA-115-21 crystals extend to $^{87}\text{Sr}/^{86}\text{Sr}$ values as high as those observed in plagioclase from ALIA-115-18, the ALIA-115-21 plagioclase do not extend to the low $^{87}\text{Sr}/^{86}\text{Sr}$ values observed in the ALIA-115-18 crystals. Compared to ALIA-115-18 plagioclase, a greater proportion of ALIA-115-21 LASS analyses revealed the presence of non-plagioclase inclusions or cracks; nonetheless, LASS enabled us to reject or trim such analyses (e.g., Figure 3).

ALIA-115-21-1: This plagioclase is 1.5 mm x 0.3 mm in size. This crystal has a large, Ca-rich core (An as high as 54) surrounded by a Na-rich rim (An as low as 45). The mean An content from the laser spots is 50 ± 7 (2 SD; see Supplementary Table 4), which is quite variable and lower than the other plagioclase crystals examined in this study (Figure 6). The $^{87}\text{Sr}/^{86}\text{Sr}$ ratios in this plagioclase, determined in 15 locations over two analytical sessions, extend from 0.72078 ± 0.00028 (2 SE) to 0.72232 ± 0.00021 (2 SE) (range > 2100 ppm).

ALIA-115-21-2: Plagioclase ALIA-115-21-2 is a glomerocryst of three individual plagioclase crystals; additional, smaller crystals are present, but were not analyzed. Two of the three large

crystals have notably Ca-rich cores (see Ca EPMA map in Supplementary Figure 1). This glomerocryst has the highest anorthite content of any plagioclase targeted here (64), with an average An content of 58 ± 6 (2 SD, $n = 23$) from the locations of the laser spots (Figure 6; Supplementary Table 4). Of all of the Samoan plagioclase evaluated here, ALIA-115-21-2 has the least isotopic variability (Figure 5). The mean $^{87}\text{Sr}/^{86}\text{Sr}$ of this plagioclase is 0.72216 ± 0.00026 (2 SD, $n = 23$ spots), and $^{87}\text{Sr}/^{86}\text{Sr}$ ranges from 0.72180 ± 0.00023 (2 SE) to 0.72235 ± 0.00028 (2 SE), determined in 23 locations over two analytical sessions. At 762 ppm, the range of measured $^{87}\text{Sr}/^{86}\text{Sr}$ values is approximately twice the 2 SD reproducibility achieved for the AMNH 107160 plagioclase reference material.

ALIA-115-21-3: Plagioclase ALIA-115-21-3 is a glomerocryst consisting of a larger crystal intergrown with at least two smaller crystals. The glomerocryst is approximately 2 mm x 0.5 mm in size. Each sub-crystal exhibits major-element zoning (see Supplementary Figure 1), but the anorthite content calculated at the location of each laser spot in this plagioclase shows limited variability relative to the other ALIA-115-21 plagioclase (mean An = 54 ± 2 [2 SD], $n = 20$; Supplementary Table 4). Of the three crystals from ALIA-115-21, this crystal exhibits the greatest variability in measured $^{87}\text{Sr}/^{86}\text{Sr}$ (Figure 5), with $^{87}\text{Sr}/^{86}\text{Sr}$ values ranging from 0.71982 ± 0.00031 to 0.72192 ± 0.00015 (range = 2910 ppm) obtained over two analytical sessions. There is a high- $^{87}\text{Sr}/^{86}\text{Sr}$ zone near the center of the largest crystal, but the zone is poorly defined owing to relatively few measurements with lower $^{87}\text{Sr}/^{86}\text{Sr}$ near the periphery of the crystal (Supplementary Figure 2).

3.2. Geochemical trends recorded in plagioclase.

The LASS data define a clear negative relationship between Sr and $^{87}\text{Sr}/^{86}\text{Sr}$ in the Samoan plagioclase crystals targeted. The data from the crystals separated from ALIA-115-21 define a shallower slope than the data from the ALIA-115-18 crystals, but all share the trend of higher $^{87}\text{Sr}/^{86}\text{Sr}$ at lower Sr concentration (Figure 6). The arrays formed by the plagioclase from the two lavas overlap in a common region characterized by high $^{87}\text{Sr}/^{86}\text{Sr}$. This extreme high- $^{87}\text{Sr}/^{86}\text{Sr}$ EM2 common component is more radiogenic than any Samoan whole rocks or mineral phases analyzed to date.

The presence of olivine inclusions (c. 20–30 μm) in a domain of a plagioclase that exhibits extremely radiogenic $^{87}\text{Sr}/^{86}\text{Sr}$ allows us to calculate the Mg# of the melt in equilibrium with the olivine and, by extension, the EM2 endmember sampled by the plagioclase assuming that the plagioclase and included olivine crystallized from the same portion of homogeneous melt. The composition of the EM2 endmember observed in the plagioclase is relatively evolved: the melt in equilibrium with the olivines included in plagioclase ALIA-115-18-1 has an Mg# of 46.8 ± 0.4 (2 SD). When this composition is plotted with all Samoan lavas from the ALIA-115 dredge, the common component EM2 composition anchors the high- $^{87}\text{Sr}/^{86}\text{Sr}$, low Mg# portion of the array (Figure 7). It is an assumption that the olivine grew from the same melt as the host plagioclase; the olivine may have grown from a more or less evolved melt prior to entrapment. Nonetheless, the calculated Mg# of the olivine inclusion, paired with the $^{87}\text{Sr}/^{86}\text{Sr}$ of the host plagioclase zone hosting the olivine, results in a melt composition that anchors the high- $^{87}\text{Sr}/^{86}\text{Sr}$ portion of the whole rock trend in $^{87}\text{Sr}/^{86}\text{Sr}$ -versus-Mg# space in Figure 7. This supports the hypothesis that the olivine was in equilibrium with the same liquid that crystallized the surrounding plagioclase material.

However, other trace elements analyzed here (e.g., Rb, Ba, Ti, Y, REEs) do not exhibit the same clear relationships with $^{87}\text{Sr}/^{86}\text{Sr}$; La is shown as an example in Figure 6. Similarly, the anorthite composition of the plagioclase at each laser spot does not show a relationship with $^{87}\text{Sr}/^{86}\text{Sr}$ (Figure 6).

4. Discussion

Two of the six Samoan plagioclase crystals examined here contain the most extreme EM2 signatures ($^{87}\text{Sr}/^{86}\text{Sr}$ up to 0.7224) ever observed in OIB, and these new, ultrahigh $^{87}\text{Sr}/^{86}\text{Sr}$ signatures surpass the highest values previously reported in Samoan whole rocks (up to 0.720469) and in magmatic clinopyroxene (up to 0.721630) (Jackson et al., 2007). Furthermore, five of the six plagioclase crystals have extreme $^{87}\text{Sr}/^{86}\text{Sr}$ heterogeneity (> 1500 ppm) that complements the intra-lava $^{87}\text{Sr}/^{86}\text{Sr}$ heterogeneity measured in plagioclase from mid-ocean ridge basalts (Lange et al., 2013), between olivine-hosted melt inclusions and their host OIB whole rocks (e.g., Harlou et al., 2009; Jackson and Hart, 2006; Reinhard et al., 2016, 2018; Sobolev et al., 2011), and between magmatic clinopyroxene and their host OIB whole rocks (e.g., Hanyu and Nakamura, 2000; Jackson et al., 2009; Hanyu et al., 2011).

The Samoan plagioclase presented here sample an EM2 component with a radiogenic Sr isotopic signature ($^{87}\text{Sr}/^{86}\text{Sr} = 0.7224$) more extreme than that observed in any mantle-derived oceanic lavas. Below we rule out assimilation and post-eruptive radiogenic ingrowth as processes generating the extreme radiogenic isotopic compositions, and then explore the implications of these new extreme EM compositions observed in Samoan plagioclase. In the Supplement we evaluate the $^{87}\text{Sr}/^{86}\text{Sr}$ composition of groundmass in ALIA-115-18 and ALIA-115-21 required by mass balance given the measured $^{87}\text{Sr}/^{86}\text{Sr}$ compositions of plagioclase and

cpx phenocrysts. The new extreme EM2 composition recorded in the plagioclase is calculated to be more evolved than any extreme EM2 lava examined to date from the Samoan ALIA-115 dredge, and its radiogenic $^{87}\text{Sr}/^{86}\text{Sr}$ composition requires that a higher fraction of recycled sediment was added to its source (Jackson et al., 2007).

4.1. Origin of $^{87}\text{Sr}/^{86}\text{Sr}$ heterogeneity in Samoan plagioclase.

The observation of intra-crystal $^{87}\text{Sr}/^{86}\text{Sr}$ disequilibrium in OIB is one of the salient findings of this study. Therefore, it is important to consider the mechanisms that may have been responsible for generating the $^{87}\text{Sr}/^{86}\text{Sr}$ heterogeneity in the plagioclase crystals we studied.

Varying degrees of radiogenic ingrowth of ^{87}Sr due to post-eruptive ^{87}Rb decay in the plagioclase cannot generate the extreme $^{87}\text{Sr}/^{86}\text{Sr}$ heterogeneity in the plagioclase crystals we measured. The lowest (0.00052) and highest (0.0068) measured Rb/Sr ratios from any two ALIA-115 plagioclase spots would lead to $^{87}\text{Sr}/^{86}\text{Sr}$ differences in the plagioclase of only 2 ppm over the 5.3 Myr (Koppers et al., 2008) since the plagioclase formed. Radiogenic ingrowth is thus not the mechanism responsible for generating $^{87}\text{Sr}/^{86}\text{Sr}$ variability in these plagioclase crystals.

Assimilation of altered oceanic crust is not likely to have generated the extreme high $^{87}\text{Sr}/^{86}\text{Sr}$ observed in the Samoan plagioclase (which have $^{87}\text{Sr}/^{86}\text{Sr} \geq 0.71788$; see Supplementary Table 4), as the $^{87}\text{Sr}/^{86}\text{Sr}$ signature of altered oceanic crust only rarely achieves $^{87}\text{Sr}/^{86}\text{Sr}$ values that approach or exceed (e.g., Hauff et al., 2003), the value of seawater ($^{87}\text{Sr}/^{86}\text{Sr} = 0.709164$; renormalized from Mokadem et al., 2015). Similarly, assimilation of modern sediments is not likely to have generated the extreme $^{87}\text{Sr}/^{86}\text{Sr}$ signatures observed here: lead is highly enriched in marine sediments (Plank and Langmuir, 1998) compared to oceanic lavas

(Willbold and Stracke, 2006), so sediment assimilation would have a disproportionate influence on the Pb isotopic composition of a lava. This is notable because the Samoan EM2 lavas from ALIA dredge 115 form an array in $\Delta^{207}\text{Pb}/^{204}\text{Pb}-\Delta^{208}\text{Pb}/^{204}\text{Pb}$ space that diverges away from the field formed by modern sediments (Figure 4 of Jackson et al., 2007), and the extreme EM2 lavas with the highest $^{87}\text{Sr}/^{86}\text{Sr}$ plot farthest from the field defined by sediments in this Pb isotopic space. This observation suggests that the assimilation of modern sediments cannot have generated the enriched $^{87}\text{Sr}/^{86}\text{Sr}$ signatures in the whole rocks and, by extension, their plagioclase cargo.

One possible mechanism for generating intra-crystal $^{87}\text{Sr}/^{86}\text{Sr}$ heterogeneity may be mixing of two (or more) isotopically distinct melts. Textural features in the plagioclase support this hypothesis: plagioclase ALIA-115-18-1 (which exhibits the second most extreme degree of intra-crystal $^{87}\text{Sr}/^{86}\text{Sr}$ variability) has a rounded and resorbed core surrounded by a narrow olivine-bearing zone (Figure 4), features consistent with magma mixing. The magmatic plagioclase targeted in this study exhibit $^{87}\text{Sr}/^{86}\text{Sr}$ zoning to varying degrees (Supplementary Figure 2); the simplest explanation for this observation is that the mixing of isotopically distinct magmas is responsible for the observed isotopic zonation. Furthermore, plagioclase crystals from each lava examined here define a different negatively sloping array in $^{87}\text{Sr}/^{86}\text{Sr}-\text{Sr}$ space (Figure 6), and a key observation is that the arrays overlap at a common high- $^{87}\text{Sr}/^{86}\text{Sr}$ EM2 component. If mixing was responsible for generating these converging arrays, one or more low- $^{87}\text{Sr}/^{86}\text{Sr}$ endmembers (with higher Sr concentrations) may have mixed with a common high- $^{87}\text{Sr}/^{86}\text{Sr}$ component to generate the negatively sloping trend observed in Figure 6. An important issue to address is the petrological characteristics of the magmas that mixed to generate the trends observed in Figure 6.

4.2. A new extreme EM2 signature in an evolved melt: evidence for mixing an evolved EM2 magma with less-evolved magmas with lower $^{87}\text{Sr}/^{86}\text{Sr}$.

Fortuitously, olivine (mean Fo = 74.5 ± 0.8 , 2 SD) included in plagioclase ALIA-115-18-1—within a zone characterized by high $^{87}\text{Sr}/^{86}\text{Sr}$ —allow us to calculate the Mg# of the EM2 common component magma to be Mg# = 46.8 ± 0.4 (2 SD). Therefore, we infer that the extreme EM2 lava from which the olivine and plagioclase crystallized was relatively evolved. For comparison, a primary melt in equilibrium with Fo₉₀ mantle olivine has a Mg# of 73.

This is an important observation because the calculated composition of the EM2 common component lies on an extension of the trend defined by the ALIA-115 whole rocks in $^{87}\text{Sr}/^{86}\text{Sr}$ –Mg# space (Figure 7): the new extreme EM2 common component has an even lower calculated Mg# and higher measured $^{87}\text{Sr}/^{86}\text{Sr}$ signature ($^{87}\text{Sr}/^{86}\text{Sr} = 0.72194 \pm 0.00057$ [2 SD, n = 4 spots]) than recorded in ALIA-115 whole-rock lavas. Because all of the lavas that form the compositional array in Figure 7 are from the same submarine dredge site off the coast of Savai'i island and presumably are petrogenetically linked, we explore a mechanism to explain the observed relationship between $^{87}\text{Sr}/^{86}\text{Sr}$ and Mg#.

We propose a conceptual model that mirrors the mechanism for formation of the $^{87}\text{Sr}/^{86}\text{Sr}$ –Sr trend illustrated in Figure 6: binary mixing of an evolved high- $^{87}\text{Sr}/^{86}\text{Sr}$ EM2 melt and a less evolved low- $^{87}\text{Sr}/^{86}\text{Sr}$ melt (right panel of Figure 7). In the model, two geochemically distinct primary mantle melts must be generated, one with low $^{87}\text{Sr}/^{86}\text{Sr}$ and one with high $^{87}\text{Sr}/^{86}\text{Sr}$. However, none of the lavas from the ALIA-115 dredge are primary melts (i.e., all lavas from ALIA dredge 115 have a Mg# of ≤ 65), so they have experienced variable degrees of magmatic evolution in the crust prior to eruption. In this dredge, the high- $^{87}\text{Sr}/^{86}\text{Sr}$ lavas are

more evolved than the low- $^{87}\text{Sr}/^{86}\text{Sr}$ lavas, as indicated in Figure 7 (left panel). Thus, in the model, a more evolved high- $^{87}\text{Sr}/^{86}\text{Sr}$ melt and a less evolved low- $^{87}\text{Sr}/^{86}\text{Sr}$ melt mix in varying proportions, producing an array of intermediate compositions. The ALIA dredge 115 lavas and the extreme EM2 common component sampled by the Samoan plagioclase in this study define a trend in $^{87}\text{Sr}/^{86}\text{Sr}$ -Mg# space that is consistent with this conceptual model (Figure 7).

This model may also explain why plagioclase $^{86}\text{Sr}/^{86}\text{Sr}$ is negatively correlated with Sr in Figure 6: the more-radiogenic mixing endmember is more evolved and is more likely to have experienced greater degrees of plagioclase fractionation. Owing to the compatibility of Sr in plagioclase, the removal of plagioclase from the most-evolved EM2 melts results in residual melt with lower Sr, whereas the less-evolved lavas with lower $^{87}\text{Sr}/^{86}\text{Sr}$ will have higher Sr concentrations. Although plagioclase fractionation exerts a powerful lever on magmatic Sr concentrations, the concentrations of other trace elements examined in this study will not be as strongly influenced by fractional crystallization of plagioclase (or olivine and clinopyroxene, the other phases identified in ALIA-115 lavas; Koppers et al., 2011). As a result, these other trace elements will not follow the same trends as Sr during magmatic evolution, thereby decoupling $^{86}\text{Sr}/^{86}\text{Sr}$ from incompatible trace-element signatures other than that of Sr. This mechanism may explain the lack of clear correlations between $^{87}\text{Sr}/^{86}\text{Sr}$ and other geochemical indicators. Alternatively, the clear relationship between $^{87}\text{Sr}/^{86}\text{Sr}$ and Sr concentrations—but not other trace-element concentrations (e.g., La in Figure 6)—may be explained by different cation diffusion rates in plagioclase (e.g., Cherniak, 2003). This is because diffusion may relax original geochemical profiles in the plagioclase to varying degrees during residence in a magma chamber (see Supplementary Discussion), a process that may preserve relationships between $^{87}\text{Sr}/^{86}\text{Sr}$ and

Sr (due to similar diffusion rates of Sr and Sr-isotopic signatures in plagioclase) while decoupling $^{87}\text{Sr}/^{86}\text{Sr}$ from other trace elements.

One remaining uncertainty concerns whether the EM2 endmember melt is universally evolved. Although the extreme EM2 mixing endmember sampled by the plagioclase is more evolved than other lavas from the Samoan dredge ALIA-115 locality (Figure 7), it is not clear whether all EM2 lavas with extreme high $^{87}\text{Sr}/^{86}\text{Sr}$ ratios should be evolved. Figure 7 (right panel) posits that a mafic parental melt for the extreme EM2 melt sampled by the ALIA-115-18 and ALIA-115-21 plagioclase existed, but this is uncertain. Mafic extreme EM2 lavas, if they exist, would enhance our understanding of this mantle endmember because they would enable investigation of primary melt phase equilibria and estimates of the temperature and pressure conditions of EM2 mantle melting.

4.3 Generation of an extreme EM2 composition via terrigenous sediment recycling

The high- $^{87}\text{Sr}/^{86}\text{Sr}$ signature identified in the most extreme EM2 Samoan ALIA-115 lavas has been interpreted to reflect the ancient recycling of upper continental crust-derived sediment subducted into the mantle (Jackson et al., 2007; White and Hofmann, 1982; Workman et al., 2008). Combining trace-element and isotopic constraints, Jackson et al. (2007) estimated that the terrigenous sediment protolith contributing to the Samoan EM2 mantle has an $^{87}\text{Sr}/^{86}\text{Sr}$ composition of 0.7421 (assuming an upper continental crust Sr concentration of 320 ppm; Rudnick and Gao, 2003). They found that the addition of ~5% of a terrigenous sediment protolith to a depleted peridotite source such as that calculated for the most geochemically depleted lavas in Samoa ($^{87}\text{Sr}/^{86}\text{Sr} = 0.704650$ and Sr concentration = 28.3 ppm; Jackson et al., 2007), could generate the geochemically enriched trace-element and $^{87}\text{Sr}/^{86}\text{Sr}$ signatures in the

second most extreme EM2 lava from Samoa, ALIA-115-18 (Jackson et al., 2007). Using the same model parameters employed by these authors, we calculate that approximately 7% sediment (i.e., an additional 2%) is required to generate the highest-measured plagioclase $^{87}\text{Sr}/^{86}\text{Sr}$ value (0.72239 ± 0.00027 ; 2 SE) reported in this study.

The bulk of marine sediment is derived from the continents: an estimated 76 wt % of marine sediment has a terrigenous origin (Plank and Langmuir, 1998). Thus, subduction of marine sediment contributes a continental signature to the mantle. Over geologic time, significant volumes of sediment have been introduced into the terrestrial mantle; recent sediment subduction flux estimates range from $1.0 \text{ km}^3 \text{ a}^{-1}$ (von Huene and Scholl, 1991) to $1.65 \text{ km}^3 \text{ a}^{-1}$ (Clift et al., 2009). We estimate the net mass of sediment that has been added to Earth's mantle over geologic time as follows. We assume a sediment density of 2500 kg m^{-3} , use the lower sediment subduction flux estimate of von Huene and Scholl (1991), and assume that 90% of all subducting sediment is relaminated to the base of the continents (Hacker et al., 2011). Using a time of 3 Ga (Shirey and Richardson, 2011), we calculate that $7.5 \cdot 10^{20} \text{ kg}$ of sediment has been added to the convecting mantle. This quantity of sediment is $\sim 0.02\%$ of the mantle by mass (however, if continents were smaller in the past, the total volume of material eroded would have been smaller). Although this quantity of subducted sediment is minor in terms of its mass fraction, it has an outsized geochemical importance: if we assume that the non-sediment portion of the mantle has the primitive composition proposed by McDonough and Sun (1995) and the sediment has a composition like GLOSS (Plank and Langmuir, 1998), then 1.4–1.9% of the most incompatible elements (Rb, Th, U, and K) are hosted in the subducted sediment domain, and 0.3–0.4% of the moderately incompatible elements (e.g., Sr and Nd) are hosted in this domain. This estimate gives a lower limit on the geochemical impact of sediment subduction on the

incompatible-element budget of the mantle because the mantle has been partially depleted by the extraction of continental crust and the average composition of the mantle today must therefore be more depleted than the primitive mantle. Assuming a simple model wherein the bulk mantle is 33% DMM and 67% primitive mantle by mass (Workman and Hart, 2005), 1.9–2.7% of the most incompatible elements and 0.5–1.2% of the moderately incompatible elements are hosted in the subducted sediment domain. The degree to which the recycled sediment domain is enriched in incompatible elements depends on the bulk mantle composition that is assumed; however, these estimates illustrate that sediment may play an important role in the geochemical budgets of highly incompatible elements.

Although 0.02% of the mass of the mantle may consist of recycled sediment, this sediment component is heterogeneously distributed: approximately 7% of the mantle source of the extreme EM2 domain sampled by the plagioclase in this study consists of recycled sediment based on geochemical constraints. The survival of such sediment-rich domains in the mantle suggests that subducted sediment is not always efficiently mixed in the dynamically convecting mantle, and therefore, geochemical signatures imparted by subducted sediment are not efficiently attenuated. Instead, regions of the mantle can contain relatively high mass fractions of recycled sediment.

There is evidence that subducted sediment is concentrated in certain regions of Earth's mantle: Castillo (1988) found that hotspots exhibiting EM (enriched mantle) signatures are positioned above one of the two near-antipodal large low-shear-velocity provinces (LLSVPs) at the base of the mantle. This finding is supported by a more recent study that investigated the link between the positioning of hotspots relative to LLSVPs and the geochemical enrichment observed in OIB at oceanic hotspots globally (Jackson et al., 2018). If EM domains trace their

origins to subducted sediment, the LLSVPs may represent regions that host unusually high concentrations of subducted sediment. LLSVPs may compose up to 7.7% of the mantle by mass (the "majority estimate" of Cottaar and Lekic, 2016), and if most of the subducted sediment is hosted in the LLSVPs, approximately 0.25% of the LLSVPs is composed of subducted sediment. This percentage is higher if, the fraction of the mass fraction of the LLSVPs has been overestimated, or if the fraction of sediment that escapes relamination is higher. Nonetheless, the high mass fraction of sediment estimated in the Samoan extreme EM2 source (~7%) is anomalous: it reflects an unusual surviving relic of subducted sediment in the dynamically convecting mantle.

Conclusions

We report new $^{87}\text{Sr}/^{86}\text{Sr}$ measurements of plagioclase in extreme Samoan EM2 lavas. We employ laser-ablation split-stream mass spectrometry (LASS), which permits simultaneous analysis of trace-element concentrations and $^{87}\text{Sr}/^{86}\text{Sr}$ from the same crystal volume. We measure over 5000 ppm of intra-crystal $^{87}\text{Sr}/^{86}\text{Sr}$ heterogeneity in two of the six plagioclase samples examined here, which is significantly greater than the long-term analytical reproducibility achieved for a plagioclase reference material (± 350 ppm). Critically, we observe highly radiogenic $^{87}\text{Sr}/^{86}\text{Sr}$ ratios (up to 0.7224) in plagioclase from two different Samoan EM2 lavas, the highest $^{87}\text{Sr}/^{86}\text{Sr}$ ratios ever measured in oceanic lavas.

The simultaneous measurement of Sr isotopic and trace-element compositions of the plagioclase reveals a relationship between $^{87}\text{Sr}/^{86}\text{Sr}$ and Sr concentrations in the six plagioclase crystals analyzed here: data from the plagioclase crystals overlap at a common enriched EM2 component in $^{87}\text{Sr}/^{86}\text{Sr}$ –Sr space. We interpret $^{87}\text{Sr}/^{86}\text{Sr}$ heterogeneity in the plagioclase—and the

relationship between $^{87}\text{Sr}/^{86}\text{Sr}$ and Sr concentrations—to reflect mixing between an evolved extremely enriched EM2 "common component" with at least one component that is less evolved and has less radiogenic $^{87}\text{Sr}/^{86}\text{Sr}$. We calculate the Mg# of this extreme EM2 common component from the compositions of olivines (forsterite content 74.5 ± 0.8 , 2 SD) hosted in a high- $^{87}\text{Sr}/^{86}\text{Sr}$ plagioclase zone that samples the EM2 common component: a melt in equilibrium with the olivines has a Mg# of 46.8 ± 0.4 (2 SD). This new calculated EM2 endmember composition plots on an extension of the negatively sloping array formed by relevant Samoan whole-rock lavas in $^{87}\text{Sr}/^{86}\text{Sr}$ –Mg# space, supporting the contention that extreme EM2 melts in Samoa are relatively evolved.

The discovery of a new extreme EM2 endmember composition provides a new estimate of the amount of recycled terrigenous sediment sampled by an EM2 melt. The elevated $^{87}\text{Sr}/^{86}\text{Sr}$ recorded in Samoan plagioclase zones requires a high fraction of recycled sediment (~7%) in the Samoan mantle source. This fraction is significantly higher than our estimate for the fraction of Earth's mantle that is likely to be composed of recycled sediment (0.02%). The observation of a new extreme EM2 signature in plagioclase from the Samoan hotspot thus provides new insights on sediment recycling, an important process for generating heterogeneity in Earth's dynamic mantle.

Acknowledgements. We thank Catherine Chauvel and one anonymous reviewer for their constructive reviews that greatly improved this manuscript, and Frédéric Moynier for editorial handling. MAE acknowledges fellowship support from the UCSB Earth Research Institute. MGJ acknowledges support from National Science Foundation grants EAR-1624840, OCE-1736984 and EAR-1347377. Discussions with Roberta Rudnick and comments on an earlier version of

this manuscript were exceedingly helpful. Helpful advice regarding sample preparation and mass spectrometry from Andrew Reinhard is gratefully acknowledged. We thank Casey Saenger for donating a portion of modern sclerosponge from Pear Tree Bottom, Jamaica.

References

- Castillo, P., 1988. The Dupal anomaly as a trace of the upwelling lower mantle. *Nature* 336, 667–670. <https://doi.org/10.1038/336667a0>
- Cherniak, D.J., 2003. REE diffusion in feldspar. *Chem. Geol.* 193, 25–41. [https://doi.org/10.1016/S0009-2541\(02\)00246-2](https://doi.org/10.1016/S0009-2541(02)00246-2)
- Christensen, J.N., Halliday, A.N., Lee, D.-C., Hall, C.M., 1995. In situ Sr isotopic analysis by laser ablation. *Earth Planet. Sci. Lett.* 136, 79–85.
- Clift, P.D., Vannucchi, P., Morgan, J.P., 2009. Crustal redistribution, crust-mantle recycling and Phanerozoic evolution of the continental crust. *Earth-Science Rev.* 97, 80–104. <https://doi.org/10.1016/j.earscirev.2009.10.003>
- Cottaar, S., Lekic, V., 2016. Morphology of seismically slow lower-mantle structures. *Geophys. J. Int.* 207, 1122–1136. <https://doi.org/10.1093/gji/ggw324>
- Davidson, J.P., Morgan, D.J., Charlier, B.L.A., Harlou, R., Hora, J.M., 2007. Microsampling and Isotopic Analysis of Igneous Rocks: Implications for the Study of Magmatic Systems. *Annu. Rev. Earth Planet. Sci.* 35, 273–311. [https://doi.org/10.1146/annurev.earth.35.031306.1402110084-6597/07/0530-0273\\$20.00](https://doi.org/10.1146/annurev.earth.35.031306.1402110084-6597/07/0530-0273$20.00)
- Davidson, J.P., Tepley, F.J., 1997. Recharge in volcanic systems: Evidence from isotope profiles of phenocrysts. *Science* (80-.). 275, 826–829. <https://doi.org/10.1126/science.275.5301.826>
- Font, L., Davidson, J.P., Pearson, D.G., Nowell, G.M., Jerram, D.A., Ottley, C.J., 2008. Sr and Pb isotope micro-analysis of plagioclase crystals from skye lavas: An insight into open-system processes in a flood basalt province. *J. Petrol.* 49, 1449–1471. <https://doi.org/10.1093/petrology/egn032>
- Garapić, G., Jackson, M.G., Hauri, E.H., Hart, S.R., Farley, K.A., Blusztajn, J.S., Woodhead, J.D., 2015. A radiogenic isotopic (He-Sr-Nd-Pb-Os) study of lavas from the Pitcairn hotspot: Implications for the origin of EM-1 (enriched mantle 1). *Lithos* 228–229, 1–11. <https://doi.org/10.1016/j.lithos.2015.04.010>
- Gast, P.W., Tilton, G.R., Hedge, C., 1964. Isotopic Composition of Lead and Strontium from Ascension and Gough Islands. *Science* (80-.). 145, 1181–1185.
- Hacker, B.R., Kelemen, P.B., Behn, M.D., 2011. Differentiation of the continental crust by relamination. *Earth Planet. Sci. Lett.* 307, 501–516. <https://doi.org/10.1016/j.epsl.2011.05.024>
- Hanyu, T., Nakamura, E., 2000. Constraints on HIMU and EM by Sr and Nd isotopes re-examined. *Earth, Planets Sp.* 52, 61–70. <https://doi.org/10.1186/BF03351614>
- Hanyu, T., Tatsumi, Y., Senda, R., Miyazaki, T., Chang, Q., Hirahara, Y., Takahashi, T.,

- Kawabata, H., Suzuki, K., Kimura, J.I., Nakai, S., 2011. Geochemical characteristics and origin of the HIMU reservoir: A possible mantle plume source in the lower mantle. *Geochemistry, Geophys. Geosystems* 12, 1–30. <https://doi.org/10.1029/2010GC003252>
- Harlou, R., Pearson, D.G., Nowell, G.M., Ottley, C.J., Davidson, J.P., 2009. Combined Sr isotope and trace element analysis of melt inclusions at sub-ng levels using micro-milling, TIMS and ICPMS. *Chem. Geol.* 260, 254–268. <https://doi.org/10.1016/j.chemgeo.2008.12.020>
- Hart, S.R., Schilling, J.-G., Powell, J.L., 1973. Basalts from Iceland and Along the Reykjanes Ridge: Sr Isotope Geochemistry. *Nature* 246, 104–107. <https://doi.org/10.1038/10.1038/physci246104a0>
- Haufl, F., Hoernle, K., Schmidt, A., 2003. Sr-Nd-Pb composition of Mesozoic Pacific oceanic crust (Site 1149 and 801, ODP Leg 185): Implications for alteration of ocean crust and the input into the Izu-Bonin-Mariana subduction system. *Geochemistry, Geophys. Geosystems* 4. <https://doi.org/10.1029/2002GC000421>
- Hofmann, A.W., 1997. Mantle geochemistry: the message from oceanic volcanism. *Nature* 385, 219–229.
- Jackson, M.G., Becker, T.W., Konter, J.G., 2018. Geochemistry and Distribution of Recycled Domains in the Mantle Inferred From Nd and Pb Isotopes in Oceanic Hot Spots: Implications for Storage in the Large Low Shear Wave Velocity Provinces. *Geochemistry, Geophysics, Geosystems*. 9. <https://doi.org/10.1029/2018GC007552>
- Jackson, M.G., Hart, S.R., 2006. Strontium isotopes in melt inclusions from Samoan basalts: Implications for heterogeneity in the Samoan plume. *Earth Planet. Sci. Lett.* 245, 260–277. <https://doi.org/10.1016/j.epsl.2006.02.040>
- Jackson, M.G., Hart, S.R., Koppers, A.A.P., Staudigel, H., Konter, J., Blusztajn, J., Kurz, M., Russell, J.A., 2007. The return of subducted continental crust in Samoan lavas. *Nature* 448, 684–687. <https://doi.org/10.1038/nature06048>
- Jackson, M.G., Hart, S.R., Shimizu, N., Blusztajn, J.S., 2009. The $^{87}\text{Sr}/^{86}\text{Sr}$ and $^{143}\text{Nd}/^{144}\text{Nd}$ disequilibrium between Polynesian hot spot lavas and the clinopyroxenes they host: Evidence complementing isotopic disequilibrium in melt inclusions. *Geochemistry, Geophys. Geosystems* 10. <https://doi.org/10.1029/2008GC002324>
- Jochum, K.P., Wilson, S.A., Abouchami, W., Amini, M., Chmeleff, J., Eisenhauer, A., Hegner, E., Iaccheri, L.M., Kieffer, B., Krause, J., McDonough, W.F., Mertz-Kraus, R., Raczek, I., Rudnick, R.L., Scholz, D., Steinhofel, G., Stoll, B., Stracke, A., Tonarini, S., Weis, D., Weis, U., Woodhead, J.D., 2011. GSD-1G and MPI-DING Reference Glasses for In Situ and Bulk Isotopic Determination. *Geostand. Geoanalytical Res.* 35, 193–226. <https://doi.org/10.1111/j.1751-908X.2010.00114.x>
- Konter, J.G., Storm, L.P., 2014. High precision $^{87}\text{Sr}/^{86}\text{Sr}$ measurements by MC-ICP-MS, simultaneously solving for Kr interferences and mass-based fractionation. *Chem. Geol.* 385, 26–34. <https://doi.org/10.1016/j.chemgeo.2014.07.009>
- Koppers, A.A.P., Russell, J.A., Jackson, M.G., Konter, J., Staudigel, H., Hart, S.R., 2008. Samoa reinstated as a primary hotspot trail. *Geology* 36, 435–438. <https://doi.org/10.1130/G24630A.1>
- Koppers, A.A., Russell, J.A., Roberts, J., Jackson, M.G., Konter, J.G., Wright, D.J., Staudigel, H. and Hart, S.R., 2011. Age systematics of two young en echelon Samoan volcanic

- trails. *Geochemistry, Geophysics, Geosystems*, 12(7).
<https://doi.org/10.1029/2010GC003438>
- Kylander-Clark, A.R.C., Hacker, B.R., Cottle, J.M., 2013. Laser-ablation split-stream ICP petrochronology. *Chem. Geol.* 345, 99–112.
<https://doi.org/10.1016/j.chemgeo.2013.02.019>
- Lange, A.E., Nielsen, R.L., Tepley, F.J., Kent, A.J.R., 2013. Diverse sr isotope signatures preserved in mid-oceanic-ridge basalt plagioclase. *Geology* 41, 279–282.
<https://doi.org/10.1130/G33739.1>
- Mcdonough, W.F., Sun, S. -s., 1995. The chemical composition of the Earth. *Chem. Geol.* 120, 223–253. [https://doi.org/10.1016/0009-2541\(94\)00140-4](https://doi.org/10.1016/0009-2541(94)00140-4)
- Miyazaki, T., Hanyu, T., Kimura, J.I., Senda, R., Vaglarov, B.S., Chang, Q., Hirahara, Y., Takahashi, T., Kawabata, H., Sato, T., 2018. Clinopyroxene and bulk rock Sr–Nd–Hf–Pb isotope compositions of Raivavae ocean island basalts: Does clinopyroxene record early stage magma chamber processes? *Chem. Geol.* 482, 18–31.
<https://doi.org/10.1016/j.chemgeo.2017.12.015>
- Mokadem, F., Parkinson, I.J., Hathorne, E.C., Anand, P., Allen, J.T., Burton, K.W., 2015. High-precision radiogenic strontium isotope measurements of the modern and glacial ocean: Limits on glacial-interglacial variations in continental weathering. *Earth Planet. Sci. Lett.* 415, 111–120. <https://doi.org/10.1016/j.epsl.2015.01.036>
- Paul, B., Woodhead, J.D., Hergt, J., Danyushevsky, L., Kunihiro, T., Nakamura, E., 2011. Melt inclusion Pb-isotope analysis by LA-MC-ICPMS: Assessment of analytical performance and application to OIB genesis. *Chem. Geol.* 289, 210–223.
<https://doi.org/10.1016/j.chemgeo.2011.08.005>
- Plank, T., Langmuir, C.H., 1998. The chemical composition of subducting sediment and its consequences for the crust and mantle. *Chem. Geol.* 145, 325–394.
[https://doi.org/10.1016/S0009-2541\(97\)00150-2](https://doi.org/10.1016/S0009-2541(97)00150-2)
- Ramos, F.C., Wolff, J. a., Tollstrup, D.L., 2005. Sr isotope disequilibrium in Columbia River flood basalts: Evidence for rapid shallow-level open-system processes. *Geology* 33, 457. <https://doi.org/10.1130/G21512.1>
- Reinhard, A.A., Jackson, M.G., Harvey, J., Brown, C., Koornneef, J.M., 2016. Extreme differences in $^{87}\text{Sr}/^{86}\text{Sr}$ between Samoan lavas and the magmatic olivines they host: Evidence for highly heterogeneous $^{87}\text{Sr}/^{86}\text{Sr}$ in the magmatic plumbing system sourcing a single lava. *Chem. Geol.* 439, 120–131.
<https://doi.org/10.1016/j.chemgeo.2016.05.017>
- Reinhard, A.A., Jackson, M.G., Koornneef, J.M., Rose-Koga, E.F., Blusztajn, J., Konter, J.G., Koga, K.T., Wallace, P.J., Harvey, J., 2018. Sr and Nd isotopic compositions of individual olivine-hosted melt inclusions from Hawai'i and Samoa: Implications for the origin of isotopic heterogeneity in melt inclusions from OIB lavas. *Chem. Geol.* 495, 36–49.
<https://doi.org/10.1016/j.chemgeo.2018.07.034>
- Roeder, P.L., Emslie, R.F., 1970. Olivine-liquid equilibrium. *Contrib. to Mineral. Petrol.* 29, 275–289. <https://doi.org/10.1007/BF00371276>
- Rudnick, R.L., Gao, S., 2003. 3.01 - Composition of the Continental Crust. *Treatise on Geochemistry* 1, 1–64. <https://doi.org/http://dx.doi.org/10.1016/B0-08-043751-6/03016-4>
- Saal, A.E., Hart, S.R., Shimizu, N., Hauri, E.H., Layne, G.D., 1998. Pb isotopic variability in melt inclusions from oceanic island basalts, Polynesia. *Science* (80-.). 282, 1481–1484.

- Shirey, S.B., Richardson, S.H., 2011. Start of the Wilson cycle at 3 Ga shown by diamonds from subcontinental mantle. *Science* (80-.). 333, 434–436. <https://doi.org/10.1126/science.1206275>
- Sobolev, A. V., Hofmann, A.W., Jochum, K.P., Kuzmin, D. V., Stoll, B., 2011. A young source for the Hawaiian plume. *Nature* 476, 434–439. <https://doi.org/10.1038/nature10321>
- Stracke, A., 2012. Earth's heterogeneous mantle: A product of convection-driven interaction between crust and mantle. *Chem. Geol.* 330–331, 274–299. <https://doi.org/10.1016/j.chemgeo.2012.08.007>
- von Huene, R., Scholl, D.W., 1991. Observations at convergent margins concerning sediment subduction, erosion, and the growth of continental crust. *Rev. Geophys.* 29, 279–316. <https://doi.org/10.1029/91RG00969>
- White, W., Hofmann, A., 1982. Sr and Nd isotope geochemistry of oceanic basalts and mantle evolution. *Nature* 296, 821–825. <https://doi.org/10.1038/296821a0>
- White, W.M., 2015. Isotopes, DUPAL, LLSVPs, and Anekantavada. *Chem. Geol.* 419, 10–28. <https://doi.org/10.1016/j.chemgeo.2015.09.026>
- Willbold, M., Stracke, A., 2006. Trace element composition of mantle end-members: Implications for recycling of oceanic and upper and lower continental crust. *Geochemistry, Geophys. Geosystems* 7, 1–30. <https://doi.org/10.1029/2005GC001005>
- Workman, R.K., Eiler, J.M., Hart, S.R., Jackson, M.G., 2008. Oxygen isotopes in Samoan lavas: Confirmation of continent recycling. *Geology* 36, 551–554. <https://doi.org/10.1130/G24558A.1>
- Workman, R.K., Hart, S.R., 2005. Major and trace element composition of the depleted MORB mantle (DMM). *Earth Planet. Sci. Lett.* 231, 53–72. <https://doi.org/10.1016/j.epsl.2004.12.005>
- Workman, R.K., Hart, S.R., Jackson, M., Regelous, M., Farley, K.A., Blusztajn, J., Kurz, M., Staudigel, H., 2004. Recycled metasomatized lithosphere as the origin of the Enriched Mantle II (EM2) end-member: Evidence from the Samoan Volcanic Chain. *Geochemistry, Geophys. Geosystems* 5, 1–44. <https://doi.org/10.1029/2003GC000623>
- Yurimoto, H., Kogiso, T., Abe, K., Barszczus, H.G., Utsunomiya, A., Maruyama, S., 2004. Lead isotopic compositions in olivine-hosted melt inclusions from HIMU basalts and possible link to sulfide components. *Phys. Earth Planet. Inter.* 146, 231–242. <https://doi.org/10.1016/j.pepi.2003.08.013>
- Zindler, A., Hart, S.R., 1986. Chemical Geodynamics. *Annu. Rev. Earth Planet. Sci.* 14, 493–571. <https://doi.org/10.1146/annurev.earth.14.1.493>

Figure Captions

Figure 1. Map of western Samoa showing the islands of Savai'i (left) and Upolu (right). The inset shows the location of the Samoan chain in the western Pacific. The location of ALIA dredge 115 is indicated (the dredge location is from Jackson et al., 2007). The map was made with GeoMapApp using the GMRT 3.5 DEM. The contour interval is 200 m, and the contour corresponding to an elevation of 0 m is bolded.

Figure 2. Global ocean island basalt and mid-ocean ridge basalt isotopic array (“mantle array”) in $^{143}\text{Nd}/^{144}\text{Nd}$ - $^{87}\text{Sr}/^{86}\text{Sr}$ space. Data are from the compilation of Stracke et al. (2003), with additional Samoan isotopic data from Workman et al. (2004) and Jackson et al. (2007). ALIA dredge 115 lavas are shown in red, with ALIA-115-18 and ALIA-115-21 whole rocks annotated. We investigate the compositions of plagioclase crystals from these two whole rock lavas in this study.

Figure 3. Demonstration of the utility of LASS for generating plagioclase-specific Sr isotopic data. In this analysis (spot 51 from crystal ALIA-115-18-2 in Supplementary Table 4), an inclusion of unknown affinity is encountered during the latter portion of the analysis. The inclusion is characterized by elevated Fe, REE (Nd is shown as an example), and Rb concentrations. The $^{87}\text{Sr}/^{86}\text{Sr}$ ratio is impacted by this inclusion, but simultaneous collection of major- and trace-element data via LASS allows us to reject the inclusion-influenced data. The figure shows counts per second (cps) for each element rather than concentration (in ppm) because the ^{43}Ca used as an internal standard is not the same in the plagioclase and the inclusion.

Figure 4. Quantitative Ca concentration map (left), $^{87}\text{Sr}/^{86}\text{Sr}$ model surface (middle), and Sr concentration model surface (right) for plagioclase ALIA-115-18-1. The Ca EPMA map was produced using Probe for EPMA and CalcImage (Probe Software, Inc.), and the $^{87}\text{Sr}/^{86}\text{Sr}$ and Sr concentration surfaces were generated using Matlab[®] (see Supplementary Methods). In each image, the location of the laser spots is indicated by circles with sizes corresponding to the laser spot size (see Supplementary Figure 1 for the Ca map with laser spot numbers added). The four olivine inclusions measured by EPMA spot analyses are indicated with red numbers in the EPMA image (see Table 1 for the olivine compositions). The olivines occur just outside of the rounded and resorbed core within a zone referred to in the text as the “olivine-bearing zone”, which corresponds to high $^{87}\text{Sr}/^{86}\text{Sr}$ (and thus the plagioclase in this olivine-bearing zone samples the extreme EM2 “common component” shown in Figure 6). The boundary between the core and the rest of the crystal (the “core-mantle boundary”) is visible as an irregular yellow line (owing to elevated Ca concentration) in the left panel. Lines indicating the crystal’s edge and the “core-mantle boundary” are drawn on the model surfaces in the middle and right panels. Analogous figures for the other five Samoan plagioclase crystals from this study are shown in Supplementary Figure 2, and EPMA elemental maps for other major elements (Si, Al, Na, etc.) are shown in Supplementary Figure 1.

Figure 5. LASS $^{87}\text{Sr}/^{86}\text{Sr}$ data from the six Samoan plagioclase targeted in this study (see Supplementary Table 4 for the $^{87}\text{Sr}/^{86}\text{Sr}$ values and uncertainties used to make the figure). Error bars are internal 2SE. Whole-rock (Jackson et al. [2007]) and cpx (Jackson et al. [2009]) values from each lava (shown as squares) are plotted adjacent to the respective plagioclase data.

Figure 6. Samoan plagioclase data from this study plotted in $^{87}\text{Sr}/^{86}\text{Sr}$ -Sr space (top panel), $^{87}\text{Sr}/^{86}\text{Sr}$ -La space (middle panel), and $^{87}\text{Sr}/^{86}\text{Sr}$ -anorthite space (lower panel). The four analyses from the olivine-bearing zone in plagioclase ALIA-115-18-1 are shown with yellow outlines. We selected the “olivine-bearing zone” plagioclase analyses by choosing laser spots from the zone nearest the olivine inclusions. We avoided laser spots that overlap with or contact the resorption surface itself because these analyses capture both the high- $^{87}\text{Sr}/^{86}\text{Sr}$ zone of the crystal and the low- $^{87}\text{Sr}/^{86}\text{Sr}$ core (and thus only four laser spot analyses are used to define the $^{87}\text{Sr}/^{86}\text{Sr}$ of the olivine zone). The four analyses from the olivine-bearing zone are circled in the top panel with a dashed yellow line, and the region encompassed by the yellow oval corresponds with the common region of overlap between the plagioclase crystals from ALIA-115-18 and the crystals from ALIA-115-21. $^{87}\text{Sr}/^{86}\text{Sr}$, Sr, and La error bars on the datapoints are internal 2 SE. Error bars for the long-term reproducibility of $^{87}\text{Sr}/^{86}\text{Sr}$ (± 363 ppm, 2 SD, for plagioclase reference material AMNH 107160, $n = 73$ analyses; Supplementary Table 3), Sr ($\pm 9.5\%$, 2 SD, for plagioclase reference material T21, $n = 95$ analyses; Supplementary Table 3) and La ($\pm 11.7\%$, 2 SD, for plagioclase reference material T21, $n = 95$ analyses; Supplementary Table 3) are shown in the lower right portion of the top two panels. Anorthite ($\text{An} = \text{molar Ca}/[\text{Ca}+\text{Na}] \cdot 100$) compositions are averages calculated from quantitative EPMA maps of each plagioclase crystal (see Supplementary Figure 1 for EPMA maps). The anorthite error bars are calculated by propagating one standard deviation of the Na and Ca measurements at the location of each laser spot. All data shown in the figure are reported in Supplementary Table 4.

Figure 7. Left panel: $^{87}\text{Sr}/^{86}\text{Sr}$ plotted against Mg# of ALIA dredge 115 whole-rock lavas. A red triangle (with yellow outline) representing the olivine-bearing zone from plagioclase ALIA-115-

18-1 is also plotted: the $^{87}\text{Sr}/^{86}\text{Sr}$ value for the olivine-bearing zone from ALIA-115-18-1 is the mean measured $^{87}\text{Sr}/^{86}\text{Sr}$ value (0.72194 ± 0.00057 , 2 SD) of four laser spots (numbers 29, 48, 57, and 73; see Supplementary Table 4) near the olivine-bearing zone in this crystal that target the high- $^{87}\text{Sr}/^{86}\text{Sr}$ zone with the olivine inclusions; the Mg# (46.8 ± 0.4 , 2 SD) shown for the olivine-bearing zone is a melt calculated to be in equilibrium with the average forsterite content (74.5 ± 0.8 , 2 SD) measured by EPMA in four olivine inclusions (see Table 1 for olivine compositions and Figure 4 for an image of ALIA-115-18-1 with the olivine locations annotated). The Mg# calculation assumes an olivine-melt Fe–Mg K_D of 0.30 ± 0.03 (Roeder and Emslie, 1970). The Mg# error bars represent 10% uncertainty in the partition coefficient. The Mg# shown for whole-rock lavas assumes that 90% of total Fe is Fe^{2+} . ALIA dredge 115 whole-rock data are from Jackson et al. (2007). Right panel: a conceptual model to explain the trend in the left panel. In this model, two isotopically distinct primary mantle melts are generated (step 1). Each of the endmember melts evolves to a lower Mg#; however, the melt with more radiogenic $^{87}\text{Sr}/^{86}\text{Sr}$ achieves a lower Mg# than the melt with lower $^{87}\text{Sr}/^{86}\text{Sr}$ (step 2; see Discussion). Finally, the two different melts mix to produce the trend seen in the left panel of this figure (step 3).

Supplementary Methods

Sample preparation

Sample preparation was performed at the University of California at Santa Barbara (UCSB). Hand samples were cut to expose fresh surfaces, plagioclase crystals were visually identified, and rock chips containing the plagioclase crystals were isolated using a small tile saw and a 150 μm diameter diamond-wire saw. The isolated chips were mounted in one-inch epoxy rounds, ground flat with progressively finer silicon carbide abrasive paper, and polished with diamond polishing compounds until a 0.25 μm finish was achieved. After polishing, the mounts were coated with approximately 20 nm of carbon (following EPMA analysis and prior to LASS analysis, this carbon coating was removed).

EPMA mapping and spot analysis

Maps of X-ray intensity for each plagioclase crystal were generated by electron probe microanalysis (EPMA) using a Cameca SX-100 instrument at UCSB. The instrument was operated at 15 kV accelerating voltage and 200 nA beam current focused to a 2 μm diameter spot. X-ray intensity was measured on a grid with 4x4 μm spacing and a dwell time of 200 ms per grid point. All X-ray intensities were mapped using wavelength-dispersive spectrometers. EPMA quantitative elemental maps of Al, Ca, Na, Si, K, Fe, Mg, P, Sr, and Ti were calculated from raw X-ray intensity maps using Probe for EPMA and CalcImage (Probe Software, Inc.) (see maps in Supplementary Figure 1). Quantification of the maps was performed using a full matrix correction for each pixel, and using a mean atomic number background method (Donovan and Tingle, 1996). The quantitative EPMA maps were used to guide laser spot placement, and the plagioclase compositions corresponding to the location of each laser spot were calculated by

extracting the relevant pixels from the quantitative maps using CalcImage, Surfer[®] (Golden Software, LLC) and MATLAB[®] (The MathWorks, Inc.) (see Supplementary Table 4).

The major-element compositions of two ⁸⁷Sr/⁸⁶Sr reference materials, T21 homogenized plagioclase and AMNH 107160, were also determined by EPMA. Both materials have homogeneous major-element (Supplementary Table 1) compositions. For both T21 and AMNH 107160, we used the Ca concentrations measured by EPMA (reported in Supplementary Table 1) as the internal standard when calculating trace-element concentrations.

In one plagioclase crystal, ALIA-115-18-1, the compositions of olivine inclusions hosted within the plagioclase were determined using EPMA spot analyses. EPMA operating parameters during spot analysis consisted of a 40-degree takeoff angle, a 20 keV beam energy, a 40 nA beam current, and a 5 μm diameter beam. The EPMA analytical standards were synthetic MnO for Mn, Fe₂SiO₄ (synthetic fayalite) for Fe, Ni₂SiO₄ (synthetic) for Ni, Mg₂SiO₄ (synthetic magnesian olivine) for Mg and Si, Chesterman Diopside for Ca, MAD-10 Orthoclase for Al, and Chromite (UC # 523-9) for Cr. Nickel, Mn, Ca, Al, and Cr X-ray intensities were measured simultaneously using 5 wavelength-dispersive spectrometers, and contemporaneous Mg, Fe, and Si X-ray intensities were measured using an energy-dispersive spectrometer. Results for each olivine are the average of 1 to 5 spots depending on the size of the olivine inclusion available for EPMA (Table 1); some olivines were cracked, limiting the surface area available for analysis. Oxygen was calculated by cation stoichiometry and was included in the matrix correction. The mass absorption coefficients used for matrix correction are from the FFAST dataset, and the Phi-rho-Z correction followed the method of Pouchou and Pichoir (1991).

LA-MC-ICP-MS

During $^{87}\text{Sr}/^{86}\text{Sr}$ analysis, the Faraday cups in the Nu Plasma HR mass spectrometer were configured to cover the Sr mass range and the intermediate half-masses to monitor the presence of doubly charged REE (Supplementary Table 5). Due to the extremely low abundances of the relevant interfering REE $^{++}$ ($^{168}\text{Yb}^{++}$ and $^{168}\text{Er}^{++}$ on mass 84, $^{170}\text{Yb}^{++}$ and $^{170}\text{Er}^{++}$ on mass 85, $^{172}\text{Yb}^{++}$ on mass 86, $^{174}\text{Yb}^{++}$ on mass 87, and $^{176}\text{Yb}^{++}$ and $^{176}\text{Lu}^{++}$ on mass 88) in plagioclase relative to the high Sr abundances (see Supplementary Table 4), we did not perform a REE $^{++}$ correction using the half-mass signal intensities. We measured all baselines 0.7 AMU below the mass of interest (Jackson and Hart, 2006), and used an ESA deflection of the beam during baseline acquisition to obtain an “instrument zero”. “On-peak” baselines were not used because we correct for Kr interference using the approach of Konter and Storm (2014) described below. Thus, we do not use the measured ^{82}Kr and ^{83}Kr intensities to make the correction for isobaric interferences from Kr, but we do report ^{83}Kr intensities in Supplementary Table 4 to demonstrate that Kr intensities were low (maximum ^{83}Kr intensity = 463 μV for any analysis; Supplementary Table 2) during the analytical sessions.

The $^{87}\text{Sr}/^{86}\text{Sr}$ and trace-element compositions of samples and reference materials were measured in analytical blocks consisting of two baseline measurements, a series of primary and secondary reference materials measured at the beginning and end of each block, and alternating samples and reference materials throughout each block. Analytical blocks ranged from 40 to 83 analyses over the course of the study. With the laser off, baselines were measured for 60 seconds at the beginning and end of each block (where a block consists of analyses of multiple plagioclase and primary/secondary reference materials); during a baseline measurement, the magnet was again moved to its off-mass position and the beam was deflected using the ESA. A “working baseline” was interpolated throughout the block, and this baseline was applied to all

analyses made during that block. After baseline measurement, the magnet was adjusted so the beam is in on-mass position to begin analysis of samples and reference materials. Samples and reference materials were then pre-ablated with a single pulse of the laser using the same spot size as used for analysis. Each pre-ablation was followed by a 45-second washout, followed by 30–45 seconds of sample analysis per laser spot. The sample stage was then moved to a subsequent spot where pre-ablation commenced after 5 seconds. The laser repetition rate and spot size varied depending on the concentration of Sr in the analyte: spot sizes ranged from 35 to 155 μm and repetition rates ranged from 10 to 60 Hz (laser spot sizes and repetition rates for all analyses are given in Supplementary Tables 3 and 4).

The Kr correction approach of Konter and Storm (2014) was employed because it effectively corrects for the isobaric interferences of Kr and Rb (the two most important interferences when measuring $^{87}\text{Sr}/^{86}\text{Sr}$ ratios; Ramos et al., 2004; Vroon et al., 2008) and for mass fractionation. Using baseline-corrected signal intensities, this method simultaneously solves for Kr and Sr mass fractionation to calculate the amount of Kr “peak stripping” required to account for the offset between the measured and canonical $^{84}\text{Sr}/^{88}\text{Sr}$ (0.00675476) and $^{86}\text{Sr}/^{88}\text{Sr}$ (0.1194) ratios. We use a canonical—rather than empirical— $^{84}\text{Kr}/^{86}\text{Kr}$ ratio of 3.276 for this Kr correction. Rb was monitored on mass 85, and the ^{87}Rb isobaric interference on ^{87}Sr was calculated assuming an $^{87}\text{Rb}/^{85}\text{Rb}$ ratio of 0.38571, i.e., the calculated ^{87}Rb signal intensity was subtracted from the ^{87}Sr signal to generate an interference-corrected $^{87}\text{Sr}/^{86}\text{Sr}$ ratio. Finally, this interference-corrected $^{87}\text{Sr}/^{86}\text{Sr}$ ratio was corrected for mass fractionation using the exponential law and a $^{86}\text{Sr}/^{88}\text{Sr}$ ratio of 0.1194.

All $^{87}\text{Sr}/^{86}\text{Sr}$ data were reduced using Iolite 2.5 (Paton et al., 2011). We used the Matlab function ‘gridfit’ (D’Errico, 2006) to depict the spatial distribution of $^{87}\text{Sr}/^{86}\text{Sr}$ and Sr

concentration in the Samoan plagioclase. See Figure 4 and Supplementary Figure 2 for the interpolated surfaces generated for each plagioclase crystal.

Micromilling and TIMS analysis of plagioclase to test the accuracy of $^{87}\text{Sr}/^{86}\text{Sr}$ values obtained by LASS

We tested whether measured LASS $^{87}\text{Sr}/^{86}\text{Sr}$ ratios from a natural, OIB-hosted plagioclase agree with the $^{87}\text{Sr}/^{86}\text{Sr}$ value measured on the same crystal by TIMS. We micromilled a large plagioclase crystal from Pitcairn lava Pit-16, a moderately enriched ($^{87}\text{Sr}/^{86}\text{Sr}$ of the whole rock = 0.704687) trachybasalt (Garapić et al., 2015). The Pit-16 plagioclase was determined to be isotopically homogeneous within the LASS analytical precision reported in this study: based on 19 separate spot analyses of the crystal, the Pit-16 plagioclase crystal yielded a measured $^{87}\text{Sr}/^{86}\text{Sr}$ ratio of 0.70442 ± 0.00018 (2 SD; Table 3). This crystal was micromilled at UCSB following the method of Charlier et al. (2006) with an ESI[®] Micromill. After Sr purification following standard column-chemistry separation techniques and TIMS analysis at the University of Leeds, the measured $^{87}\text{Sr}/^{86}\text{Sr}$ value of the powder was 0.704505 ± 0.000012 (2 SE; Table 2). The total Sr blank of 149 pg—the sum of the total chemistry procedural blank of 52 pg Sr, and the micromilling blank of 97 pg Sr—is insignificant relative to the estimated total Sr in the micromilled powder (approximately 49 ng). The TIMS $^{87}\text{Sr}/^{86}\text{Sr}$ value obtained for the Pit-16 micromilled powder overlaps with the mean LASS value within uncertainty, demonstrating that we are able to accurately reproduce the measured $^{87}\text{Sr}/^{86}\text{Sr}$ TIMS value of a natural plagioclase crystal using LASS.

We also micromilled a portion of the T21 homogenized plagioclase glass primary reference material and a portion of the AMNH 107160 plagioclase secondary reference material

to ensure that measured $^{87}\text{Sr}/^{86}\text{Sr}$ values obtained for micromilled powders agree with values obtained from plagioclase chips. We obtained an $^{87}\text{Sr}/^{86}\text{Sr}$ value of 0.704699 ± 0.000018 via TIMS for the T21 micromilled powder (Table 2), which is indistinguishable from the TIMS reference value of 0.704712 ± 0.000009 (2 SE) obtained by dissolution of a 4.2 mg chip of this reference material (Table 2). For the AMNH 107160 plagioclase micromilled powder, we obtained an $^{87}\text{Sr}/^{86}\text{Sr}$ value of 0.704408 ± 0.000020 (2 SE) (Table 2), which agrees within uncertainty with the TIMS reference value of 0.704386 ± 0.000008 obtained by dissolution of a 2.0 mg chip of this plagioclase (Table 2). Finally, the LASS $^{87}\text{Sr}/^{86}\text{Sr}$ values obtained for the ANMH 107160 plagioclase reference material (0.704373 ± 0.000249 , 2 SD, $n = 83$) agree with the $^{87}\text{Sr}/^{86}\text{Sr}$ values obtained on this plagioclase by TIMS for both a plagioclase chip and a micromilled powder. Thus, within analytical precision, micromilling does not influence the measured $^{87}\text{Sr}/^{86}\text{Sr}$ composition of plagioclase analyzed in this study.

LASS major- and trace-element accuracy and reproducibility

We measured the major- and trace-element composition from each laser spot via LASS. ^{43}Ca was used as the internal standard, and BHVO-2G was used as a primary reference material (reference trace-element concentrations for BHVO-2G are from Jochum et al., 2005). MPI-DING basaltic glasses ML3-B and KL-2 (reference concentrations from Jochum et al., 2006) were treated as secondary reference materials to assess data quality. We measured these geologic reference materials twice each during each block of analyses: once at the beginning, and once at the end. The LA-Q-ICP-MS concentrations for ML3-B and KL-2 are compared with the preferred concentrations in Supplementary Table 2. Additionally, the homogeneous T21 plagioclase was used as a phase-specific secondary reference material for trace element analyses

(but note that T21 was used as a primary reference material for Sr isotopic analyses; see above). Trace-element concentrations were obtained for two fragments of T21 plagioclase by wet chemistry and Q-ICP-MS at Aarhus University, Denmark, and the results, together with major-element analyses of the T21 plagioclase by EPMA, are compared with the major- and trace-element concentrations obtained by LASS in Supplementary Table 2. We also present initial trace-element concentrations obtained by LASS for the AMNH 107160 plagioclase in Supplementary Table 2, although no reference values are available at this time. The measured concentrations from each LASS analysis of these reference materials are available in Supplementary Table 3. All trace-element data were reduced in Iolite 2.5 using the “internal standard” trace-element data reduction scheme (Paton et al., 2011).

Long-term average concentrations for all elements analyzed by LASS in the basaltic glass reference materials KL2-G and ML3B-G ($n = 26$ analyses for both reference materials) agree with published reference values within 8% (Supplementary Table 2). Reproducibility for most elements analyzed by LASS for KL2-G and ML3B-G was better than 9% (2 RSD) except for Lu, with 2 RSD = 10.1% for KL2-G and 2 RSD = 11.3% for ML3B-G. Long-term average concentrations for most elements measured by LASS in the T21 homogenized plagioclase reference material ($n = 95$ analyses) agree with the preliminary reference values obtained via solution ICP-MS and EPMA within 10%. Exceptions include K and Rb, for which LASS results show only modest agreement with EPMA (for K) and solution ICP-MS (for Rb) preliminary reference values (the difference is 16% and 34%, respectively) in the T21 plagioclase. The reproducibility for most elements analyzed by LASS in T21 was better than 12 % (2 RSD) except for Sm and Gd (18%, 2 RSD), Er (24%), Yb (35%), Lu (50%) and Rb (31%). Although the reproducibility of Rb is not as good as the other elements examined here, we report measured

Rb concentrations to demonstrate that isobaric ^{87}Rb interferences on ^{87}Sr can be effectively corrected when measuring $^{87}\text{Sr}/^{86}\text{Sr}$ ratios. We emphasize that the Rb concentration measured by Q-ICP-MS, used for obtaining trace-element concentrations by LASS, was not used to correct for the interference of ^{87}Rb when measuring $^{87}\text{Sr}/^{86}\text{Sr}$ ratios (instead, the isobaric correction for ^{87}Rb on mass 87 was made using the mass 85 intensity obtained during MC-ICP-MS analysis). We also report heavy REEs that exhibit low concentrations and relatively poor analytical reproducibility for the T21 plagioclase (see Supplementary Table 2) solely to demonstrate that REE^{++} isobaric interferences in the Sr mass range are negligible for both reference materials and Samoan plagioclase samples.

Because the ALIA-115-18 and ALIA-115-21 plagioclase crystals we analyzed are not homogeneous with respect to their major-element compositions, the mean Ca concentration of the plagioclase at the location of each laser spot—determined by extraction from quantitative EPMA Ca concentration maps—was used as the internal elemental standard. However, EPMA concentrations for ALIA-115-18-2 are unavailable at the location of the laser spots from the analytical session on 5/8/2017 because this plagioclase was analyzed by LASS before an EPMA map of the crystal was prepared. For this crystal we used the mean measured Ca concentration from the locations of the laser spots from a later analytical session (8.12 ± 0.45 wt %, $n = 40$) as the internal standard for trace-element analyses from 5/8/2017 (see Supplementary Table 4).

Concentrations of a suite of elements (Si, Na, K, Fe, Mg, Al, and Sr) were determined for the Samoan plagioclase from ALIA-115-18 and ALIA-115-21 by two methods: EPMA (which uses compositions extracted from EPMA maps at the location of each laser spot) and LASS (which quantifies the elemental concentrations in the volume of crystal that was analyzed via laser ablation). The two methods measure concentrations from two different portions of the

crystal: the EPMA method gives compositions at the crystal surface targeted by the laser, whereas the LASS method provides an average composition from the crystal volume ablated by the laser. Therefore, the observation that the EPMA and LASS measurements exhibit relatively good agreement in the Samoan plagioclase (see Supplementary Table 4) suggests that downhole geochemical zonation in the Samoan plagioclase crystals does not significantly influence the geochemical data presented here.

Supplementary Discussion

Mass-balance requirements for groundmass $^{87}\text{Sr}/^{86}\text{Sr}$.

The measured $^{87}\text{Sr}/^{86}\text{Sr}$ compositions of plagioclase and clinopyroxene/clinopyroxene from ALIA-115-18 and ALIA-115-21 are generally more radiogenic than the $^{87}\text{Sr}/^{86}\text{Sr}$ of the respective whole rocks with few exceptions (Figure 5). We use the example of ALIA-115-18 to calculate the $^{87}\text{Sr}/^{86}\text{Sr}$ of the groundmass based on mass-balance requirements by using the average measured plagioclase Sr and $^{87}\text{Sr}/^{86}\text{Sr}$ (mean = 2053 $\mu\text{g g}^{-1}$ and 0.72048 respectively; this study), clinopyroxene/clinopyroxene Sr and $^{87}\text{Sr}/^{86}\text{Sr}$ (mean = 51.5 $\mu\text{g g}^{-1}$ and 0.720531 respectively; Jackson et al., 2009) and whole-rock Sr concentration and $^{87}\text{Sr}/^{86}\text{Sr}$ value (511 $\mu\text{g g}^{-1}$ and 0.718592 respectively; Jackson et al., 2007). We use the modal mineralogy of ALIA-115-18 (Koppers et al., 2011): 5% plagioclase phenocrysts, 3% clinopyroxene phenocrysts, and 92% groundmass. Given these assumptions, the calculated $^{87}\text{Sr}/^{86}\text{Sr}$ of the groundmass in ALIA-115-18 is 0.718107 (compared to a measured whole-rock value of 0.718592). Thus, the required difference between the whole-rock and groundmass $^{87}\text{Sr}/^{86}\text{Sr}$ is relatively small (675 ppm for

ALIA-115-18) despite the significantly higher $^{87}\text{Sr}/^{86}\text{Sr}$ observed in clinopyroxene and some plagioclase zones compared to whole-rock values.

Cation diffusion in plagioclase

Here, we discuss the role that diffusion may play in decoupling $^{87}\text{Sr}/^{86}\text{Sr}$ from other geochemical signatures in the Samoan plagioclase we studied. There is a strong relationship between valence state and cation diffusion rates in plagioclase, whereby univalent cations diffuse most rapidly, divalent cations diffuse at intermediate rates, and trivalent cations diffuse most slowly (Cherniak, 2003). Therefore, in plagioclase, Sr diffuses more rapidly than the trivalent REE but more slowly than the alkali elements. Strontium also diffuses significantly more rapidly than the timescales on which CaAl-NaSi interdiffusion in plagioclase occurs (Costa et al., 2003; Grove et al., 1984). There is also a relationship between ionic radius and diffusion whereby larger cations diffuse more slowly (e.g., Ba diffuses more slowly than Sr; Cherniak, 2002). Thus, if Sr zones in the plagioclase we studied have “blurred” by diffusion over magma chamber timescales, $^{87}\text{Sr}/^{86}\text{Sr}$ would not be expected to correlate with trace elements that diffuse at significantly different rates than Sr.

Although the rates of chemical and tracer (i.e., isotopic) diffusion of Sr in silicate melts differ by over an order of magnitude (Baker, 1989), similar rates of Sr chemical and tracer diffusion have been determined for plagioclase (Cherniak and Watson, 1994). Therefore, the Sr concentration and $^{87}\text{Sr}/^{86}\text{Sr}$ profiles in the plagioclase should track each other, but may be more or less diffusively relaxed than the profiles of trace elements or anorthite content. Below, we explore whether diffusion could plausibly decouple $^{87}\text{Sr}/^{86}\text{Sr}$ from other geochemical signatures

in the Samoan plagioclase in this study using previously published cation diffusion parameters and geologically reasonable estimates for temperature.

Following Cherniak (2003), we estimate the time required to lose cation zoning in plagioclase. In this approach, zones are modeled as sheets of thickness l with a different concentration of a given element than the surrounding medium. The diffusion coefficient is given by D , and time is t . Cherniak (2003) defined a dimensionless parameter ($=Dt/l^2$) that allows one to calculate the time at which concentrations in a region of a zone are changed by a certain amount. When the dimensionless parameter Dt/l^2 is equal to $3.3 \cdot 10^2$, the concentration at the center of the zone is modified by 10%. At this point, Cherniak considers a zone to be lost (2003). Although this criterion for loss of zonation is somewhat arbitrary, it provides a way to estimate the timescales required to lose plagioclase zoning for specific elements, and hence the timescales over which their geochemical signatures become decoupled by diffusion.

Given a temperature of 1000 °C, we estimate the timescales over which 100 μm zones are lost in plagioclase for various cations to evaluate whether diffusion can decouple $^{87}\text{Sr}/^{86}\text{Sr}$ from other trace-element concentrations. We use diffusion coefficients from plagioclase experiments that most closely approximate the compositions of the Samoan plagioclase in this study (i.e., labradorite), but the paucity of experimental data prevents us from choosing diffusion parameters from studies with identical plagioclase compositions and experimental procedures. We are also unable to calculate timescales of zoning loss for elements with unexplored diffusion behavior in plagioclase (although inferences from valence state and radius can be drawn).

Univalent cations diffuse most rapidly in plagioclase: 100 μm K zoning is estimated to be lost in < 1 year in $\text{An}_{62.6}$ plagioclase at 1000 °C, using the diffusion parameters of Giletti and Shanahan (1997). Although Giletti and Shanahan (1997) did not evaluate Rb diffusion in

labradorite, they determine that the diffusivities for Rb and K are similar in albite, with Rb diffusing more slowly. Divalent cations diffuse more slowly than univalent cations: for example, at 1000 °C, 100 µm Sr zones would be lost in ~10 years in An₆₇ plagioclase (Cherniak and Watson, 1994), and Ba zones would be lost in approximately 800 years in An₆₇ plagioclase at 1000 °C (Cherniak, 2002). Finally, 100 µm trivalent REE zones would be lost in ~10,000 years at 1000 °C in An₆₇ plagioclase (Cherniak, 2003). CaAl-NaSi interdiffusion proceeds even more slowly: CaAl-NaSi zones in An₈₀₋₈₁ plagioclase would be lost in ~15 Ma at 1000 °C (Grove et al., 1984).

Over shorter timescales (at a given temperature), zoning patterns in plagioclase are “blurred” rather than lost. The aforementioned dimensionless parameter Dt/l^2 describes this “blurring” when it equals $1.8 \cdot 10^{-3}$ (Cherniak, 2003). At this point, the composition of the zone 10% from its surface (i.e., at a depth of 1/10) has changed by 10%. Using the same zone size (100 µm) and temperature (1000 °C) as above, we calculate that univalent cation zones would be blurred in 17 days, Sr zones would be blurred in 0.6 years, Ba zones would be blurred in 50 years, REE zones would be blurred in 700 years, and CaAl-NaSi zones would be blurred in ~800,000 years.

Although we do not attempt to reconstruct plagioclase residence times here (see Zellmer et al., 1999), these example calculations demonstrate that at geologically reasonable timescales and temperatures, diffusion may blur zones in plagioclase at sufficiently different rates to decouple $^{87}\text{Sr}/^{86}\text{Sr}$ from other geochemical signatures (e.g., Rb, K, REE, anorthite). This observation may explain why $^{87}\text{Sr}/^{86}\text{Sr}$ does not correlate with these trace-element or major-element indices. In contrast, $^{87}\text{Sr}/^{86}\text{Sr}$ and Sr concentration signatures diffusively relax at similar

rates, a phenomenon that is perhaps responsible for preserving the trends between $^{87}\text{Sr}/^{86}\text{Sr}$ and Sr in the Samoan plagioclase we studied.

References

- Baker, D.R., 1989. Tracer vs. trace element diffusion: diffusional decoupling of Sr concentration from Sr isotope composition. *Geochim. Cosmochim. Acta* 53, 3015–3023.
- Charlier, B.L.A., Ginibre, C., Morgan, D., Nowell, G.M., Pearson, D.G., Davidson, J.P., Ottley, C.J., 2006. Methods for the microsampling and high-precision analysis of strontium and rubidium isotopes at single crystal scale for petrological and geochronological applications. *Chem. Geol.* 232, 114–133. <https://doi.org/10.1016/j.chemgeo.2006.02.015>
- Cherniak, D.J., 2003. REE diffusion in feldspar. *Chem. Geol.* 193, 25–41. [https://doi.org/10.1016/S0009-2541\(02\)00246-2](https://doi.org/10.1016/S0009-2541(02)00246-2)
- Cherniak, D.J., 2002. Ba diffusion in feldspar. *Geochim. Cosmochim. Acta* 66, 1641–1650. [https://doi.org/10.1016/S0016-7037\(01\)00866-3](https://doi.org/10.1016/S0016-7037(01)00866-3)
- Cherniak, D.J., Watson, E.B., 1994. A study of strontium diffusion in plagioclase using Rutherford backscattering spectroscopy. *Geochim. Cosmochim. Acta* 58, 5179–5190. [https://doi.org/10.1016/0016-7037\(94\)90303-4](https://doi.org/10.1016/0016-7037(94)90303-4)
- Costa, F., Chakraborty, S., Dohmen, R., 2003. Diffusion coupling between major and trace elements and a model for the calculation of magma chamber residence times using plagioclase. *Geochim. Cosmochim. Acta* 67, 2189–2200. [https://doi.org/10.1016/S0016-7037\(00\)01345-5](https://doi.org/10.1016/S0016-7037(00)01345-5)
- D’Errico, J.R., 2006. Understanding Gridfit.
- Donovan, J.J., Tingle, T.N., 1996. An Improved Mean Atomic Number Background Correction for Quantitative Microanalysis. *Microsc. Microanal.* 2, 1–7. <https://doi.org/10.1017/S1431927696210013>
- Garapić, G., Jackson, M.G., Hauri, E.H., Hart, S.R., Farley, K.A., Blusztajn, J.S., Woodhead, J.D., 2015. A radiogenic isotopic (He-Sr-Nd-Pb-Os) study of lavas from the Pitcairn hotspot: Implications for the origin of EM-1 (enriched mantle 1). *Lithos* 228–229, 1–11. <https://doi.org/10.1016/j.lithos.2015.04.010>
- Giletti, B.J., Shanahan, T.M., 1997. Alkali diffusion in plagioclase feldspar. *Chem. Geol.* 139, 3–20. [https://doi.org/10.1016/S0009-2541\(97\)00026-0](https://doi.org/10.1016/S0009-2541(97)00026-0)
- Grove, T.L., Baker, M.B., Kinzler, R.J., 1984. Coupled CaAl-NaSi diffusion in plagioclase feldspar: Experiments and applications to cooling rate speedometry. *Geochim. Cosmochim. Acta* 48, 2113–2121. [https://doi.org/10.1016/0016-7037\(84\)90391-0](https://doi.org/10.1016/0016-7037(84)90391-0)
- Jackson, M.G., Hart, S.R., 2006. Strontium isotopes in melt inclusions from Samoan basalts: Implications for heterogeneity in the Samoan plume. *Earth Planet. Sci. Lett.* 245, 260–277. <https://doi.org/10.1016/j.epsl.2006.02.040>
- Jochum, K.P., Stoll, B., Herwig, K., Willbold, M., Hofmann, A.W., Amini, M., Aarburg, S., Abouchami, W., Hellebrand, E., Mocek, B., Raczek, I., Stracke, A., Alard, O., Bouman, C., Becker, S., Dücking, M., Brätz, H., Klemm, R., De Bruin, D., Canil, D., Cornell, D., De Hoog, C.J., Dalpé, C., Danyushevsky, L., Eisenhauer, A., Gao, Y., Snow, J.E., Groschopf, N., Günther, D., Latkoczy, C., Guillong, M., Hauri, E.H., Höfer, H.E., Lahaye, Y., Horz, K.,

- Jacob, D.E., Kasemann, S.A., Kent, A.J.R., Ludwig, T., Zack, T., Mason, P.R.D., Meixner, A., Rosner, M., Misawa, K., Nash, B.P., Pfänder, J., Premo, W.R., Sun, W.D., Tiepolo, M., Vannucci, R., Vennemann, T., Wayne, D., Woodhead, J.D., 2006. MPI-DING reference glasses for in situ microanalysis: New reference values for element concentrations and isotope ratios. *Geochemistry, Geophys. Geosystems* 7. <https://doi.org/10.1029/2005GC001060>
- Jochum, K.P., Willbold, M., Raczek, I., Stoll, B., Herwig, K., 2005. Chemical Characterisation of the USGS Reference Glasses GSA-1G, GSC-1G, GSD-1G, GSE-1G, BCR-2G, BHVO-2G and BIR-1G Using EPMA, ID-TIMS, ID-ICP-MS and LA-ICP-MS. *Geostand. Geoanalytical Res.* 29, 285–302. <https://doi.org/10.1111/j.1751-908X.2005.tb00901.x>
- Konter, J.G., Storm, L.P., 2014. High precision $^{87}\text{Sr}/^{86}\text{Sr}$ measurements by MC-ICP-MS, simultaneously solving for Kr interferences and mass-based fractionation. *Chem. Geol.* 385, 26–34. <https://doi.org/10.1016/j.chemgeo.2014.07.009>
- Koppers, A.A., Russell, J.A., Roberts, J., Jackson, M.G., Konter, J.G., Wright, D.J., Staudigel, H. and Hart, S.R., 2011. Age systematics of two young en echelon Samoan volcanic trails. *Geochemistry, Geophysics, Geosystems*, 12(7). <https://doi.org/10.1029/2010GC003438>
- Paton, C., Hellstrom, J., Paul, B., Woodhead, J., Hergt, J., 2011. Iolite: Freeware for the visualisation and processing of mass spectrometric data. *J. Anal. At. Spectrom.* 26, 2508–2518. <https://doi.org/10.1039/c1ja10172b>
- Pouchou, J.-L., Pichoir, F., 1991. Quantitative analysis of homogeneous or stratified microvolumes applying the model “PAP,” in: *Electron Probe Quantitation*. Springer, pp. 31–75.
- Ramos, Frank C., John A. Wolff, and Darren L. Tollstrup. "Measuring $^{87}\text{Sr}/^{86}\text{Sr}$ variations in minerals and groundmass from basalts using LA-MC-ICPMS." *Chemical Geology* 211.1-2 (2004): 135-158. <https://doi.org/10.1016/j.chemgeo.2004.06.025>
- Vroon, P.Z., van der Wagt, B., Koornneef, J.M., Davies, G.R., 2008. Problems in obtaining precise and accurate Sr isotope analysis from geological materials using laser ablation MC-ICPMS. *Anal. Bioanal. Chem.* 390, 465–476. <https://doi.org/10.1007/s00216-007-1742-9>
- Zellmer, G.F., Blake, S., Vance, D., Hawkesworth, C., Turner, S., 1999. Plagioclase residence times at two island arc volcanoes (Kameni Islands, Santorini, and Soufriere, St. Vincent) determined by Sr diffusion systematics. *Contrib. to Mineral. Petrol.* 136, 345–357. <https://doi.org/10.1007/s004100050543>

Supplementary figure captions

Supplementary Figure 1. Quantitative EPMA concentration maps of Al, Ca, Fe, K, Mg, Na, P, Si, Sr, and Ti for the six Samoan plagioclase crystals targeted in this study. All maps were

generated via quantitative EPMA mapping using CalcImage (Probe Software, Inc.; see Supplementary Methods). The circles in each map correspond to laser spot locations and sizes, and the numbers correspond to the analysis number. We show the spot numbers of analyses that have been discarded for completeness. The geochemical data from each spot (including the average concentrations calculated from the EPMA maps, trace-element concentrations measured by LASS, and $^{87}\text{Sr}/^{86}\text{Sr}$ measured by LASS) are available in Supplementary Table 4.

Supplementary Figure 2. Quantitative Ca concentration maps (left), $^{87}\text{Sr}/^{86}\text{Sr}$ model surfaces (middle), and Sr concentration model surfaces (right) for the six Samoan plagioclase crystals targeted in this study. The Ca EPMA maps were quantified using CalcImage (Probe Software, Inc). The $^{87}\text{Sr}/^{86}\text{Sr}$ and Sr concentration surfaces were generated using the ‘gridfit’ function in Matlab[®] (see Supplementary Methods). The data used to construct the model surfaces are reported in Supplementary Table 4. The EPMA maps and model surfaces are scaled identically to enable comparisons between each panel. Similarly, the scales for Ca, $^{87}\text{Sr}/^{86}\text{Sr}$, and Sr are held constant for each crystal in order to facilitate comparisons between crystals. Therefore, a larger range in colors in a given Sr model surface corresponds to a greater range in measured $^{87}\text{Sr}/^{86}\text{Sr}$ or Sr concentration. The locations and diameters of the circles on each map correspond to locations and sizes of the laser spots. Each spot’s number shown in the Ca map corresponds to the analysis number in Supplementary Table 4.

Supplementary Figure 3. Measured (by LASS) $^{87}\text{Sr}/^{86}\text{Sr}$ of reference materials AMNH 107160, MACS-3, modern sclerosponge, and isotopically homogeneous plagioclase crystal Pit-16 (from Pitcairn Island; Garapić et al., 2015) over the course of this study. See Supplementary Table 3 for the reference material data used to make this figure. Analyses for each material are plotted in

temporal order and are grouped by analytical session. The mean $^{87}\text{Sr}/^{86}\text{Sr}$ measured by LASS of each material is shown with a solid line, and the mean ± 2 SD is shown with a dashed line. Error bars for individual LASS analyses are internal 2 SE. The reference values for each material are shown with red squares. All reference values shown are corrected to NBS987 $^{87}\text{Sr}/^{86}\text{Sr} = 0.710240$. TIMS reference values for AMNH 107160 and Pit-16 are from this study and were measured on a mineral chip and a micromilled powder, respectively (see Table 2). Because the reference values for these materials consist of one measurement by TIMS, the reported uncertainties are 2 SE. The reference value for MACS-3 comes from Jochum et al. (2011), and the modern sclerosponge value—which we assume is identical to the Sr isotopic composition of modern seawater—is from Mokadem et al. (2015). These reference values consist of multiple measurements, and the uncertainties are 2 SD. The measured LASS and reference TIMS $^{87}\text{Sr}/^{86}\text{Sr}$ values for reference materials show excellent agreement.

Figures

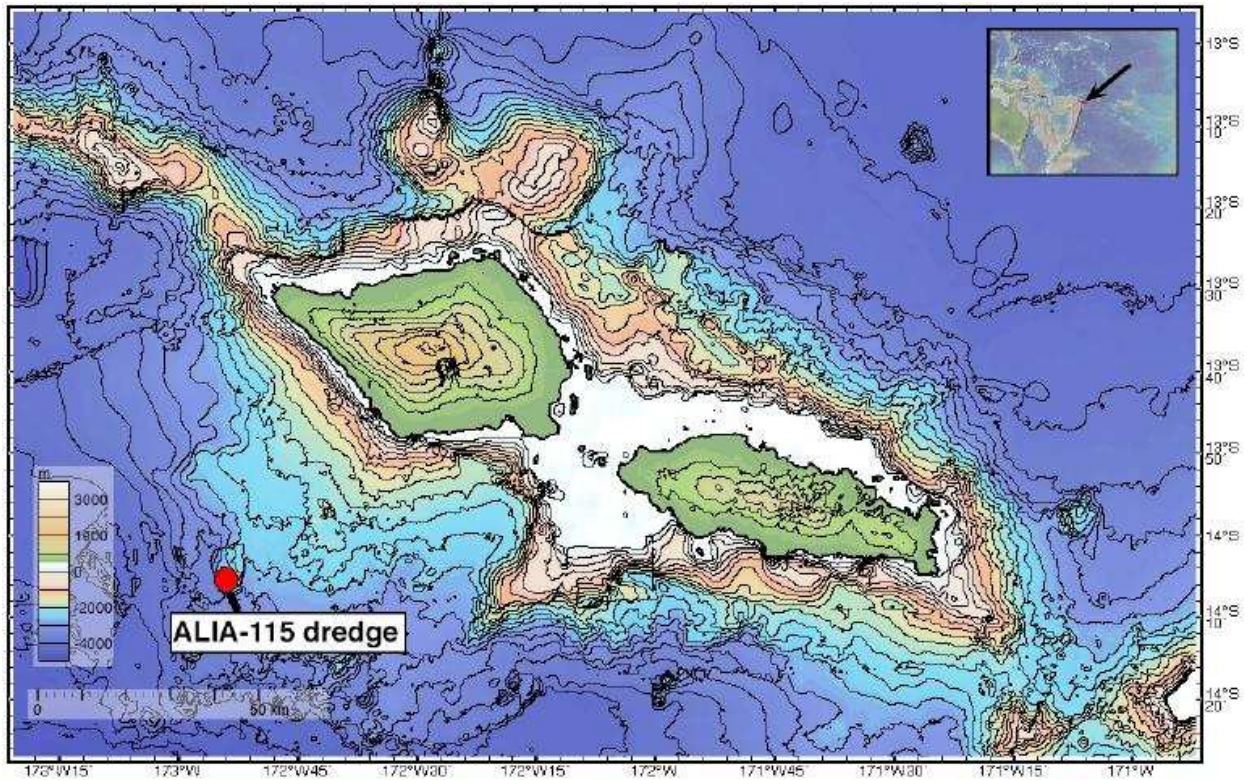


Figure 1

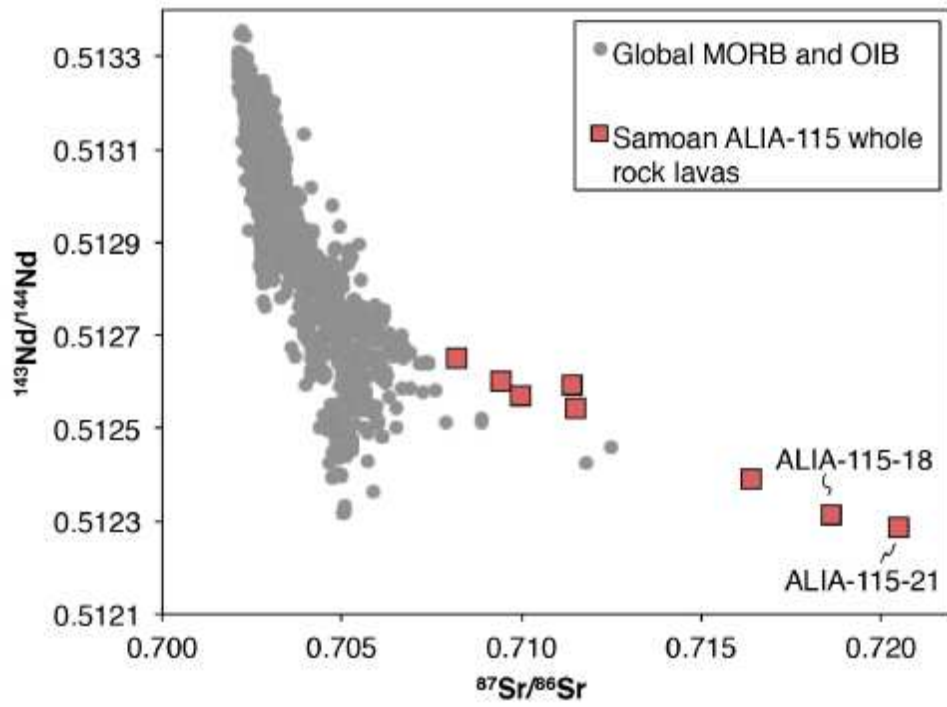


Figure 2

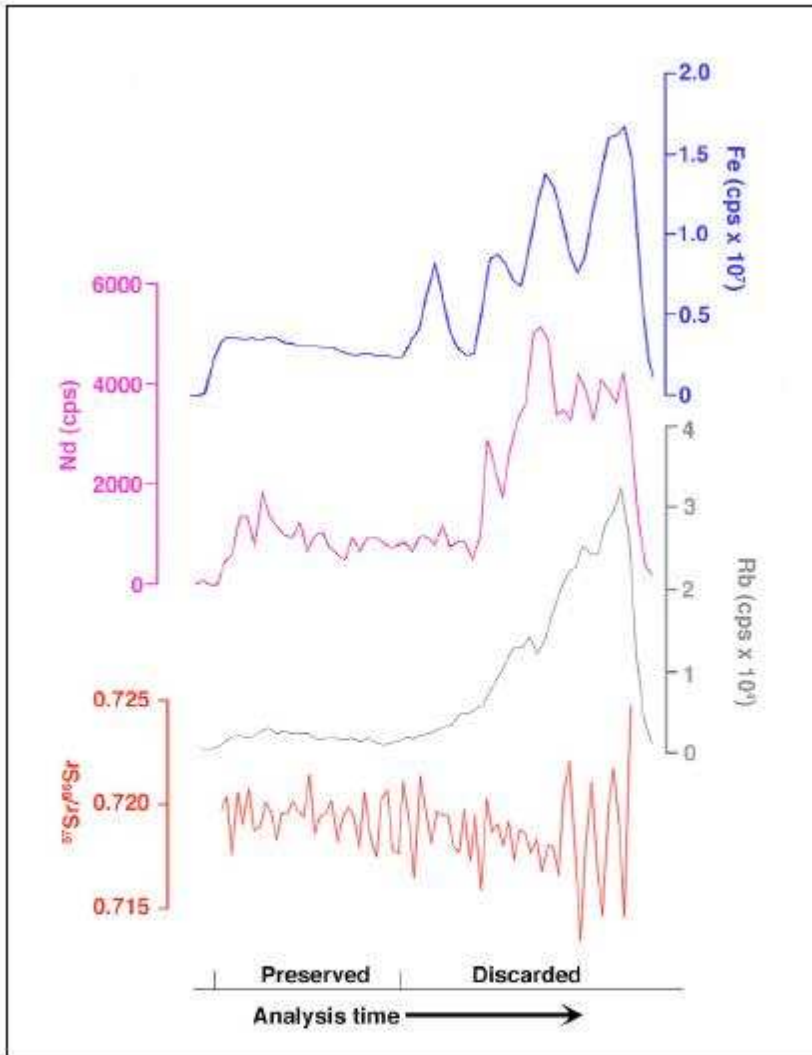


Figure 3.

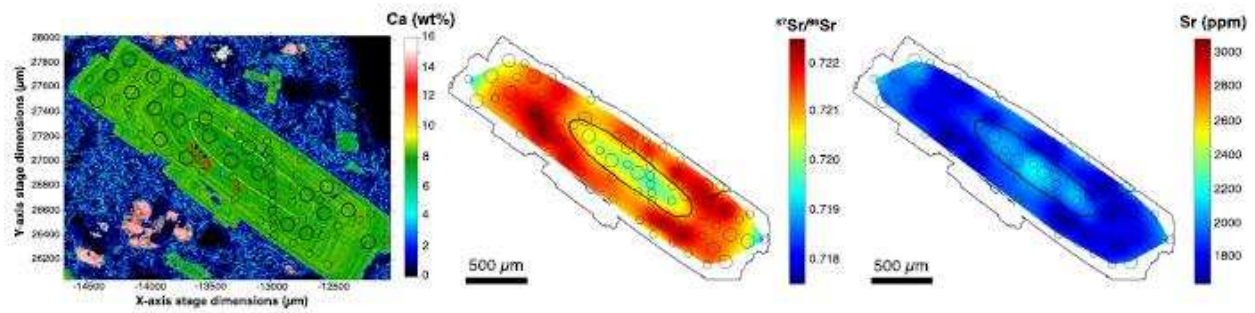


Figure 4

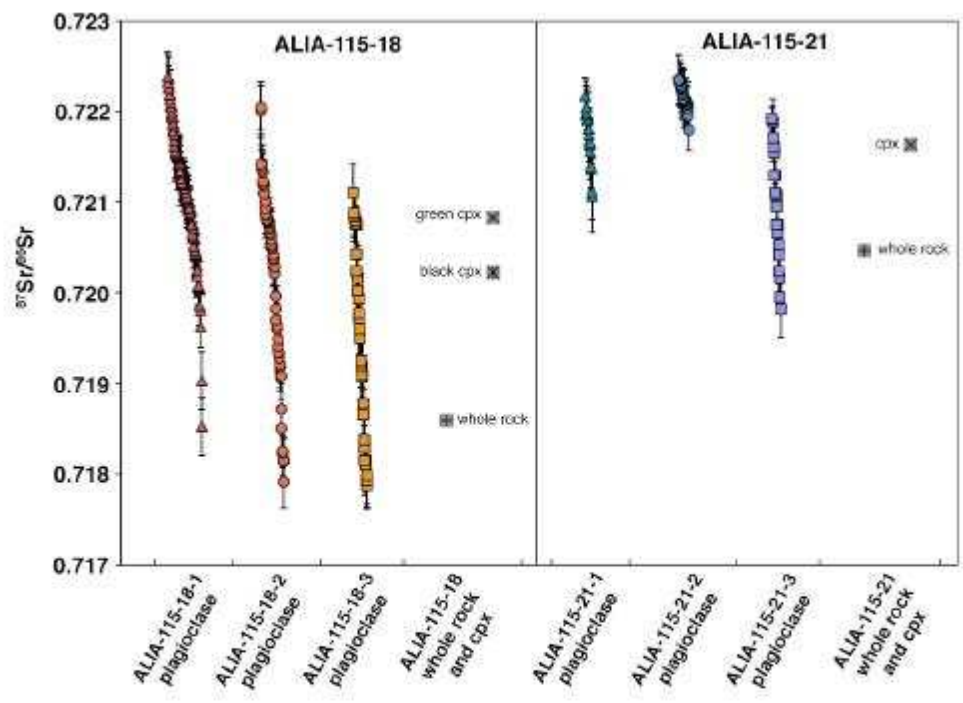


Figure 5

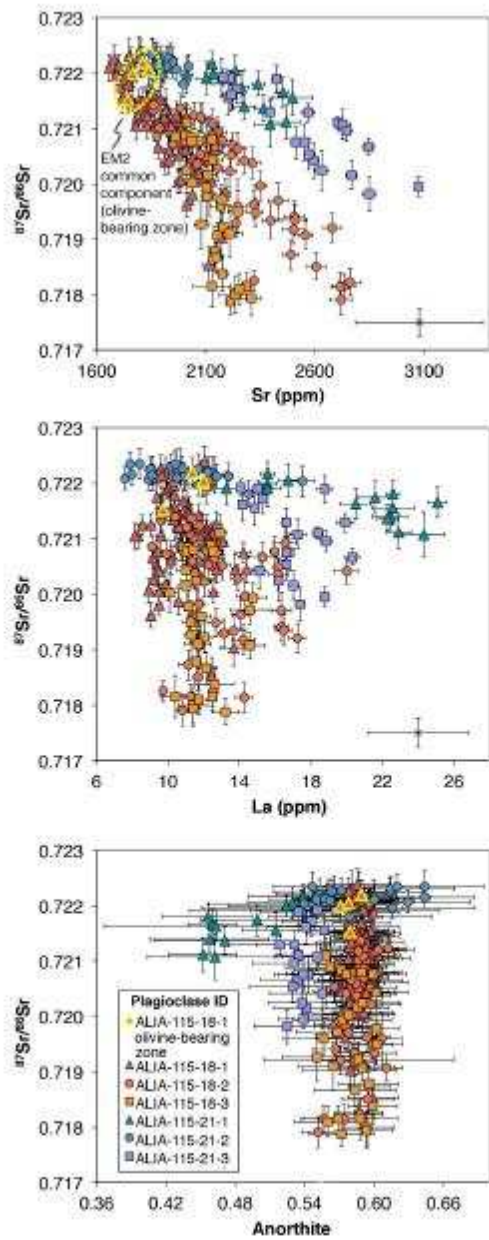


Figure 6

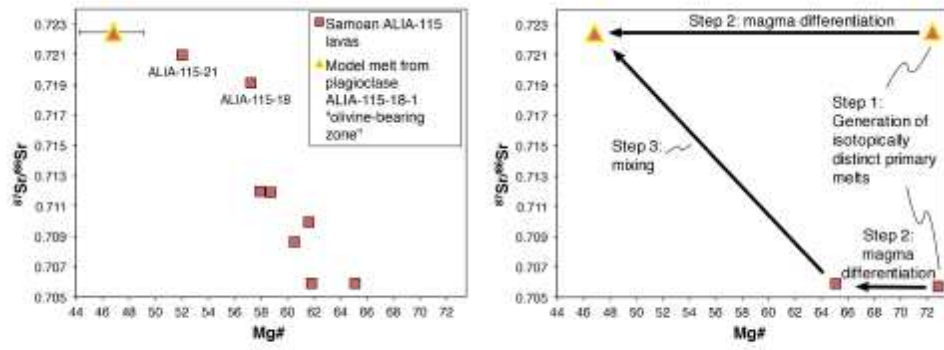


Figure 7

Table 1. Compositions of four olivines included in plagioclase ALIA-115-18-1.

	Number of spc analyses	SiO ₂ (wt.%)	2σ	MgO (wt.%)	2σ	FeO (wt.%)	2σ	NiO (wt.%)	2σ	MnO (wt.%)	2σ	Al ₂ O ₃ (wt.%)	2σ	Cr ₂ O ₃ (wt.%)	2σ	CaO (wt.%)	2σ	Total (wt.%)	Fo#	2σ
Olivine 1	5	37.76	0.42	37.38	0.40	22.98	0.12	0.11	0.01	0.31	0.01	0.02	0.01	0.01	0.02	0.28	0.02	98.86	74.36	0.27
Olivine 2	3	39.22	1.10	38.79	1.05	22.95	0.01	0.11	0.00	0.31	0.01	0.03	0.02	0.00	0.01	0.31	0.02	#####	75.08	0.50
Olivine 3	5	37.68	0.25	37.15	0.29	23.07	0.09	0.11	0.01	0.31	0.01	0.03	0.01	0.01	0.01	0.28	0.01	98.63	74.17	0.12
Olivine 4	1	37.61	n/a	37.05	n/a	22.61	n/a	0.10	n/a	0.31	n/a	0.05	n/a	0.00	n/a	0.37	n/a	98.10	74.50	n/a

Four olivines included in a zone in the ALIA-115-18-1 plagioclase crystal were analyzed by EPMA as described in the text. Each olivine was analyzed at between 1 to 5 separate spot locations. The 2 SD reproducibility of each oxide and of the calculated Fo# of olivines that were analyzed multiple times are reported.

Table 2. New TIMS analyses of reference materials in this study.

Sample name	Sample type	Estimated Sr (ng) ¹	TIMS ⁸⁷ Sr/ ⁸⁶ Sr ²	2 SE	LA-MC-ICP-MS ⁸⁷ Sr/ ⁸⁶ Sr ³	2 SD
Analyses conducted October 2015						
NBS987	Solution	-	0.710247	0.000015	-	-
BHVO-1	Powder	-	0.703503	0.000004	-	-
T21 homogenized plagioclase	Mineral fragment	-	0.704712	0.000009	-	-
Analyses conducted October 2017						
NBS987	Solution	-	0.710233	0.000014	-	-
BHVO-2	Powder	-	0.703470	0.000012	-	-
T21 homogenized plagioclase	Micromilled powder	18	0.704699	0.000018	-	-
AMNH 107160 plagioclase	Mineral fragment	-	0.704386	0.000008	0.70436	0.00026
AMNH 107160 plagioclase	Micromilled powder	15	0.704408	0.000020	0.70436	0.00026
Pit-16 plagioclase	Micromilled powder	49	0.704505	0.000012	0.70442	0.00018

¹Sr quantities for micromilled powders are estimated from the milled volume and the measured Sr concentration of each plagioclase (see Supplementary Table 2), and assume 100% recovery and a plagioclase density of 2.7 g/cm³.

²Aside from NBS987, all reported ⁸⁷Sr/⁸⁶Sr values are normalized to NBS987 ⁸⁷Sr/⁸⁶Sr = 0.710240.

³LA-MC-ICP-MS values are averages of multiple analyses over the course of this study, which are summarized in Table 3 and reported in Supplementary Table 3.

Table 3. $^{87}\text{Sr}/^{86}\text{Sr}$ values measured from geological reference materials by LA-MC-ICP-MS in this study compared to TIMS reference values.

Reference material	Mean measured $^{87}\text{Sr}/^{86}\text{Sr}$ by LA-MC-ICP-MS ¹	LA-MC-ICP-MS 2SD	LA-MC-ICP-MS 2SD (ppm)	Number of analyses	TIMS reference $^{87}\text{Sr}/^{86}\text{Sr}$ ²	TIMS reference uncertainty ³	Difference between LA-MC-ICP-MS and TIMS reference values (ppm)
AMNH 107160 plagioclase	0.70436	0.00026	363	73	0.704386	0.000008 (2SE)	-33
Pit-16 plagioclase	0.70442	0.00018	257	19	0.704505	0.000012 (2SE)	-115
USGS MACS-3 carbonate	0.70754	0.00019	270	40	0.707546	0.000004 (2SD, n=5)	-6
Modern sclerosponge	0.70916	0.00018	260	40	0.709164	0.000002 (2SD, n=17)	1

¹Refer to Supplementary Table 3 for the individual analyses used to calculate the mean measured Sr isotopic composition and uncertainties reported here.

²The reference values for AMNH 107160 plagioclase and Pit-16 plagioclase were obtained by TIMS and are reported in Table 2. The USGS MACS-3 carbonate reference value is reported in Jochum et al. (2011). The reference value for the modern sclerosponge is the modern seawater value of Mokadem et al. (2015). All reference and measured values have been normalized to NBS987 $^{87}\text{Sr}/^{86}\text{Sr}=0.710240$.

³Reference value analytical uncertainties for AMNH 107160 and Pit-16 plagioclase are 2 SE. Uncertainties for MACS-3 and modern sclerosponge—for which reference values are means of multiple ratios—are 2 SD.